NWP SAF

Satellite Application Facility for Numerical Weather Prediction

Document NWPSAF-EC-VS-014

Version 1.0

18 December 2006

SMOS Community Microwave Emission Model (SMOS-CMEM)

T.R.H. Holmes
VUA, Amsterdam

SMOS Community Microwave Emission Model (SMOS-CMEM)

T.R.H. Holmes
VUA, Amsterdam

This documentation was developed within the context of the EUMETSAT Satellite Application Facility on Numerical Weather Prediction (NWP SAF), under the Cooperation Agreement dated 16 December, 2003, between EUMETSAT and the Met Office, UK, by one or more partners within the NWP SAF. The partners in the NWP SAF are the Met Office, ECMWF, KNMI and Météo France.

SMOS Community Microwave Emission Model (SMOS-CMEM)

T.R.H. Holmes[1]

18 December 2006

[1]VUA, Amsterdam

Abstract

In 2007 / 2008 ESA plans to launch the SMOS (Soil Moisture and Ocean Salinity) satellite mission. The passive microwave radiometer will - for the first time ever - measure global microwave emission at L-band, a wavelength that has a high potential for soil moisture remote sensing. Current operational soil moisture analysis systems rely on 2 m temperature and relative humidity observations. These schemes are efficient in improving the turbulent surface fluxes but often fail to improve soil moisture itself. To incorporate future satellite observations over land in surface analysis systems new observation operators, i.e. land surface emission models, have to developed. This report describes the community microwave emission model and presents preliminary research outcomes on the calibration of CMEM and systematic and random errors of the modelled first guess.

1   Introduction

From 2007 / 2008 onwards, satellite-borne passive microwave observations at L-band will become available for the first time ever through ESA's (European Space Agency) Soil Moisture and Ocean Salinity mission (SMOS). The sensitivity of L-band measurements to soil moisture has been thoroughly analysed (e.g. Ulaby et al. (1986)) and the applicability of soil moisture retrievals has been demonstrated over the last decades (e.g. Jackson et al. (1999)). In recent years, data assimilation studies also demonstrated the potential benefit of this observation type for hydrological modelling. However, due to the lack of measurements covering large spatial scales the encouraging results were either obtained from observation system simulation experiments (OSSEs; e.g. Balsamo et al. (2006)), which make use of synthetic observations, or for field experiments at the local or regional scale (e.g Seuffert et al. (2003), Seuffert et al. (2004)). Only very few studies have been focussing on the operational use of L-band observations in numerical weather prediction (NWP) applications.

Reichle and Koster (2005) assimilated global Advanced Microwave Scanning Radiometer (AMSR) derived soil moisture fields (Njoku et al. (2003)) into NASA's (North American Space Agency) catchment land surface model using an Ensemble Kalman Filter. Comparisons against in-situ observations revealed that the analysed soil moisture fields are more accurate than the satellite product or the model fields alone. In a later study, Drusch (2006) used ECMWF's Integrated Forecast System (IFS) to quantify the impact of satellite derived soil moisture on the surface analysis and local weather parameters: Assimilating the TRMM Microwave Imager data set for the Southern United States (Gao et al. (2006)) analysed surface and root zone soil moisture were improved when compared against observations from the Oklahoma Mesonet; the corresponding turbulent surface fluxes and local weather parameters changed substantially.

In both studies derived soil moisture has been assimilated. Systematic differences between the modelled first guess and the observations were minimized through cumulative distribution function matching in a pre-processing step as described in Reichle and Koster (2004) and Drusch et al. (2005). However, for operational applications in NWP it is desirable to assimilate brightness temperatures or radiances rather than derived geophysical parameters. Within the framework of the European Land Data Assimilation Study (ELDAS) a prototype assimilation system has been developed for the single column version of the IFS (Seuffert et al. (2003), Seuffert et al. (2004)). To transfer the first guess soil moisture into observation space the land surface microwave emission model (LSMEM; Drusch et al. (2001), Gao et al. (2004)) has been coupled to the NWP model.

An optimal data assimilation system depends on a reliable description of the error statistics of the observations and the modelled first guess. In this study we will focus on three research topics:

1. Develop a community microwave emission model (CMEM) for the NWP and SMOS communities with a modular structure that allows to quantify the systematic and random errors introduced through different

parameterizations in the forward operator.

2. Quantify systematic errors in the modelled first guess and calibrate CMEM using historic L-band observations.

3. Quantify systematic and random errors based on operational NWP model output and the calibrated CMEM.

2 NWP Model Interface and CMEM Concept

In general, the observed brightness temperature at the top of the atmosphere TB_{toa} is a function of soil, vegetation, and atmospheric parameters. In NWP applications, namely DA, the forward emission model input data will mainly be obtained from the land surface component of the NWP model. An interface is needed to transform the geophysical parameters used in the NWP model into variables relevant for the radiative transfer computations. This section briefly describes the land surface scheme used in ECMWF's Integrated Forecast System and its implications on the computation of TB_{toa}.

The Tiled ECMWF Scheme for Surface Exchanges over Land (TESSEL; van den Hurk et al. (2000), Viterbo and Beljaars (1995)) is incorporated in the IFS. The soil is discretized in four layers of 0.07, 0.21, 0.72, and 1.89 m depths (from top to bottom). The soil heat transfer is described through the Fourier law of diffusion. It is assumed that heat fluxes are predominantly vertical and that the effects of phase changes in the soil and the heat transfer associated with vertical movement of water can be neglected (DeVries (1975)). At the bottom, no heat flux of energy is assumed, while at the top, the boundary condition is the soil heat flux at the surface area weighted over the tiles. The volumetric heat capacity is assumed to be constant, the heat conductivity is given by a combination of the values for the dry and the saturated heat conductivity, which is parameterized through the heat conductivity of the soil matrix and the thermal conductivity of water (Peters-Lidard et al. (1998)).

Vertical movement of water in the unsaturated zone is computed using the Richards equation and Darcy's law. Functional relationships between the hydraulic conductivity and diffusivity and soil water are specified according to Clapp and Hornberger (1978). ECMWF's land surface scheme uses a single loamy soil type for the globe and the corresponding values for volumetric soil moisture at field capacity and permanent wilting point are calculated based on the review of measurements presented by Patterson (1990). Soil moisture and soil water conductivity at saturation are obtained from Cosby et al. (1984). Values for individual parameters are summarized in Tab. 1. In order to keep the surface model as simple as possible the Integrated Forecast System is presently using only one soil type (Viterbo (1996)). A model update introducing a global data set with realistic geographical variation of the most relevant soil parameters is planned for 2007.

Each gridbox in the model is divided in up to 8 tiles (bare ground, low and high vegetation without snow, exposed snow, snow under high vegetation, interception reservoir, ocean/lakes, and sea ice). In each gridbox two vegetation classes (high and low) are present. Twenty vegetation types, including deserts, ice caps, inland water and ocean, have been defined from an external data base (U.S. Geological Survey (1999)). Each vegetation type is characterized by a set of fixed parameters for the minimum canopy resistance, spatial coverage, leaf area index, a sensitivity coefficient describing the dependence of the canopy resistance on water vapor deficit, and the root distribution over the soil layers. The fraction of a grid box covered by each of the tiles depends on the type and relative area of low and high vegetation, and the presence of snow and intercepted water. A skin temperature forms the interface between the soil and the atmosphere. It is calculated for each of the grid box tiles separately by solving the surface energy balance assuming a complete coverage of the specific tile. Although the surface is tiled, energy and water budgets are evaluated for a single atmospheric and soil profile per grid box. Further details on the surface-atmosphere coupling are given in (ECMWF (2003)).

Simplified solutions for the radiative transfer equation have been used for more than a decade to model land surface emissivities (e.g. Kerr and Njoku (1990)). When vegetation is represented as a single-scattering layer above a rough surface, the brightness temperature on top of the atmosphere TB_{toa} can be written as:

$$
\begin{aligned}
TB_{toa} = \quad & TB_{au} \quad + exp(-\tau_{atm}) \cdot TB_{ad} \cdot r_r \cdot exp(-2 \cdot \tau_{veg}) \\
+ \quad & exp(-\tau_{atm}) \cdot [T_{eff} \cdot e \cdot exp(-\tau_{veg}) + T_c \cdot (1-\omega) \cdot (1 - exp(-\tau_{veg})) \cdot (1 + r_r \cdot exp(-\tau_{veg})]
\end{aligned}
\tag{1}
$$

where TB_{au} and TB_{ad} are the up- and down-welling atmospheric brightness temperature and τ_{atm} is the atmospheric opacity calculated from the single atmospheric grid box profile. r_r is the reflectivity of the surface (equal to one minus the emissivity e), τ_{veg} the vegetation opacity and ω the single scattering albedo. T_{eff} is the effective temperature of the surface medium and the canopy temperature (T_c) is usually considered to be equal to either the T_{eff} or the air temperature.

As already mentioned earlier, model grid boxes are not uniform and can contain a variety of surface types. For the computation of the brightness temperature 7 different tile types (t) with unique radiative characteristics have been defined similar to the TESSEL tiles (a detailed description can be found in Section 3). The aggregated top-of-atmosphere brightness temperature for a grid box TB_{toa} can now be written as the sum of the emission of the individual tiles, weighted by their fractional coverage F and the atmospheric contribution for the specific grid box:

$$
TB_{toa} = TB_{au} + exp(-\tau_{atm}) \cdot \sum_{t=1}^{7} TB_{tov}(t) \cdot F(t)
\tag{2}
$$

where TB_{tov} is the top-of-vegetation emission per tile. The radiative transfer equation for TB_{tov} can be expressed in terms of the components; soil, vegetation and atmosphere:

$$
TB_{tov} = TB_{soil} \cdot exp(-\tau_{veg}) + TB_{veg} + TB_{veg} \cdot r_r \cdot exp(-\tau_{veg}) + TB_{ad} \cdot r_r \cdot exp(-2 \cdot \tau_{veg})
\tag{3}
$$

$$
TB_{soil} = T_{eff} \cdot e
\tag{4}
$$

$$
TB_{veg} = T_c \cdot (1-\omega) \cdot (1 - exp(-\tau_{veg}))
\tag{5}
$$

where TB_{soil} and TB_{veg} are the brightness temperatures from the soil and vegetation.

3 CMEM

To solve the tiled radiative transfer equation from Equation 2 we developed the Community Microwave Emission Model (CMEM), which is a hybrid version of L-MEB (Pellarin et al. (2003)) and LSMEM (Drusch et al. (2001), Gao et al. (2004)) specifically designed for data assimilation applications in NWP frameworks. This radiative transfer model comprises four **components** computing:

1. surface (TB_{soil} and r_r),

2. vegetation (TB_{veg} and τ_{veg}),

3. snow (modifications of TB_{soil} and r_r) and

4. atmosphere (TB_{au}, TB_{ad} and τ_{atm}).

Technically, each component consists of a number of **modules**. Components can be changed and configured individually. For the radiative transfer computations 7 physically unique tiles have been defined: four snow free tiles (bare soil, low vegetation, high vegetation, water) and three snow covered tiles (snow on the three land tiles). This division in tiles is similar to the TESSEL tiles, but differs in that; 1) ocean, sea ice and lakes are all part of the water tile; 2) the interception reservoir, if at all modelled, is integrated in the vegetation water content and 3) snow on bare soil is treated as a separate tile. In the following subsections the components and their individual modules are introduced.

3.1 Surface component

The surface component, calculating TB_{soil} and r_r is further divided into four sub-components that contain: dielectric models, the effective temperature, the emissivity and the roughness correction. All land surface tiles use the soil component in the same (user defined) configuration. For the water tile the dielectric constant of sea water or ice is calculated (depending on the presence of sea ice); roughness effects and foam coverage are neglected.
This section describes the optional modules for the soil component.

In this study, soil texture information is derived from the Food and Agricultural Organization of the UN data set (FAO; FAO (2000)). The FAO soil texture data are static at 10 km spatial resolution and distinguish between 3 soil texture classes (coarse, medium, fine). Sand and clay fractions have been computed from a look-up table according to Salgado (1999). Loam is the residual of $(1 - sand - clay)$. From this we derive the following texture information:

- bulk density ($BD\,[g/cm3]$) according to Hillel (1980);
  $BD = 1.6 \cdot sand + 1.1 \cdot clay + 1.2 \cdot loam$,

- porosity ($P[cm^3/cm^3]$);
  $P = \rho_b/\rho_s$, where ρ_s is the specific density,

- wilting point ($WP[cm^3/cm^3]$) according to Wang and Schmugge (1980);
  $WP = 0.06774 - 0.064 \cdot sand + 0.478 \cdot clay$

- $\alpha[-]$ from table data (Wang and Schmugge, 1980);
  $\alpha_{(fghz>2.5)} = 0$,
  $\alpha_{(fghz<=2.5)} = 100 \cdot WP$,
  $\alpha(max) = 26$

3.1.1 Effective Temperature

TB_{soil} is the emissivity times the effective temperature of the emitting soil medium (see Equation 4). T_{eff} is the sum of the physical temperatures of the emitting layers, weighted by their relative contribution to the surface emission. The Wilheit model (1978) approximates T_{eff} by a weighting function over all the soil layers, but this
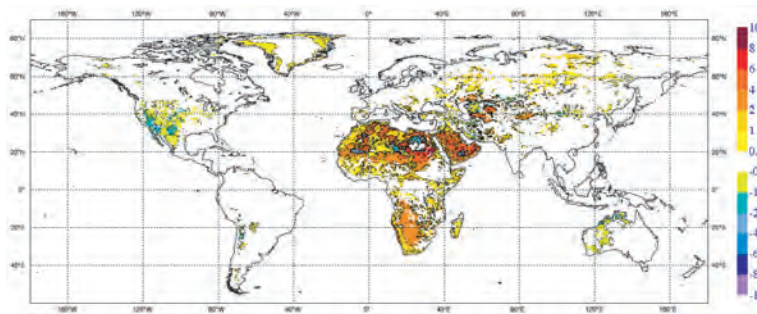
Figure 1: Difference in effective temperature as calculated by two different models; Wigneron (2001) - Wilheit (1978), and using the dielectric model of Dobson et al. (1985). In July, at 12:00 UTC, the difference reaches 8 K in the Sahara where it is day time. In Asia and the America's, there is almost no difference because the temperature gradients are small at night.

is computational expensive. To limit the cost, the T_{eff} can be parameterized based on a surface temperature ($z = 5cm$) and a deep soil temperature ($z = 50cm$):

$$T_{eff} = T_{deep} + (T_{surf} - T_{deep}) \cdot C \qquad (6)$$

The C parameter is related to the temperature sensing depth and is calibrated differently by different authors:

- Constant C-parameter (Choudhury et al., 1982), for $f = 0.6\ to\ 10\ Ghz$;

- Moisture dependant C-parameter (Wigneron et al., 2001), for $f = 1.4\ GHz$;

- Dielectric constant dependant C-parameter (Holmes et al., 2006), for $f = 1.4\ GHz$.

At L-band, the sensing depth varies over several centimeters depending on soil moisture (10 to 50cm). The model by Choudhury et al. (1982) is not soil moisture dependant. Wigneron et al. (2001) adapted the Choudhury model to account for the influence of soil moisture on the effective temperature. When the Wang dielectric model is used, the modelled sensing depth does not vary linearly with soil moisture, but by a function of the dielectric constant. The Holmes 2006 effective temperature model uses the Wang dielectric constant to model the soil moisture dependance of sensing depth. All off these parameterizations can be calibrated on the global scale to minimize the difference with the Wilheit effective temperature.

In this study, the default effective temperature model for L-band is the Wigneron model. This is because the Dobson model is used for the dielectric constant and because it is better calibrated for global applications. Figure 1 shows the difference between the effective temperature as calculated according to Wilheit and Wigneron. This shows the Wigneron model estimates the T_{eff} within 1% accuracy for most regions. Only at the middle of the day, in dry regions where temperature gradients are high, does the Wigneron model overestimate the T_{eff} by up to 3%. For higher frequencies ($f > 2.5GHz$), the Choudhury model is set as the default.

3.1.2   Dielectric models

The emissivity of the soil in the microwave range of the spectrum is highly dependant on soil moisture because of the big difference in dielectric constant (k) between water ($k = 80$) and soil particles ($k = 4$). The dielectric constant of the soil medium ε_{soil} is primarily a function of volumetric soil water content $VSWC$, temperature and soil texture. The two most commonly used semi-empirical, texture dependant, dielectric models are:
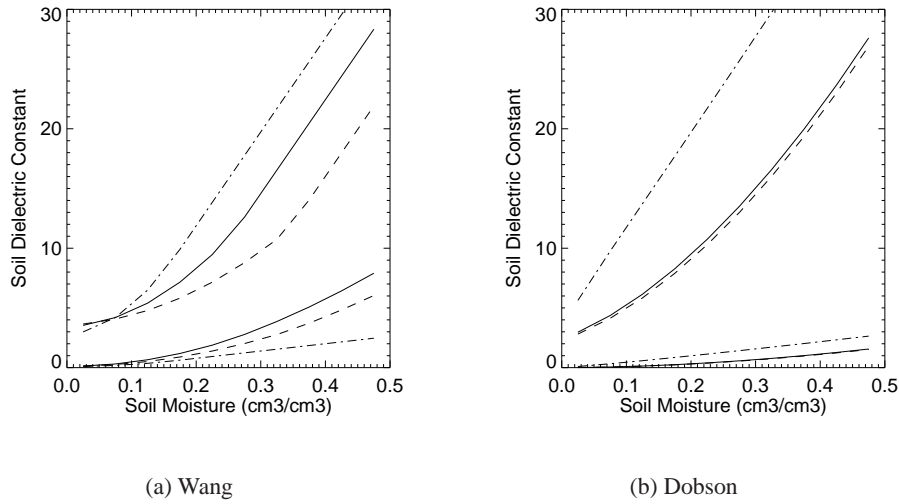
(a) Wang   (b) Dobson

Figure 2: Soil dielectric constant as a function of moisture content for different soil types; clay (dash), clay-loam (solid) and sand (dash-dot); according to a) Wang with ε_{wat} of sea; b) Dobson with ε_{wat} of soil. Both the real and the imaginary part of the dielectric constant are shown in the figure, with the real part always having a higher value.

- Wang and Schmugge (1980), calibrated for $f = 1.4 \ to \ 5 \ GHz$, distinguishes between bound water and free water and;

- Dobson et al. (1985), developed for $f = 1.4 \ to \ 18 \ GHz$.

The Wang and Schmugge model distinguishes between the bound and free water in the soil which results in a nonlinearity of dielectric constant versus volumetric soil moisture (Fig. 2). The Wang and Schmugge model needs the texture dependant parameter α for the conductivity loss factor at frequencies below 2.5 GHz. From the table data the simple relationship $\alpha = 100 \cdot WP$ is used, where WP is the wilting point of the soil.

The Dobson model is more thoroughly parameterized regarding soil texture and for a wider range in frequencies ($f = 1.4 \ to \ 18 GHz$) than the Wang and Schmugge model. At $f = 1.4 \ GHz$, it does not fully account for the dielectric properties of bound water at low moisture content (Dobson et al. (1985)). This results in an overestimation of the dielectric constant.

Matzler (1998) developed a simpler dielectric constant relation for the special case 'very dry sand':

$$\varepsilon_{soil} = 2.53 + \frac{(2.79 - 2.53)}{(1. - j \cdot (f/0.27))} + j \cdot 0.002 \tag{7}$$

where $j = 0 + 1i$ and $f[GHz]$ is the frequency. This is used in the L-MEB model and included in CMEM for the frequency range up to 10 GHz.

The choice of dielectric model changes the predicted brightness temperatures significantly (Fig. 3). Differences in regions with sandy soils can reach 20 K. The default model is the Dobson model, and Matzler's parameterization is used for very dry sand. The input fields are the $VSWC_{surf}$ and T_{eff}, except in the multi-layer model of Wilheit, which uses the temperature and moisture of the different layers directly.

Models to calculate the dielectric constant of water ε_{wat} are also included in this module. They include the pure water, saline water (see Figure 4) and soil water options:
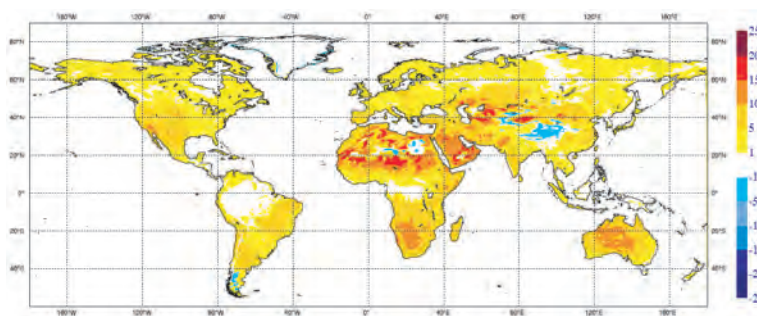
Figure 3: Difference in Brightness temperature $\Delta TB_{toa[H]}$ at $\theta = 50^o$ with $TB_{toa[H]}$ calculated using different dielectric models (Dobson et al. (1985) minus Wang and Schmugge (1980)).
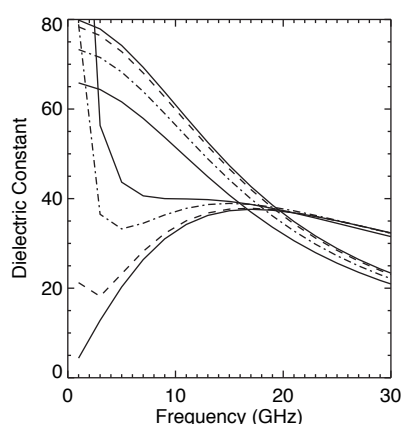

Figure 4: Dielectric constant of sea water at 20^oC at salinities of 0, 6, 30 and $60\%_o$ for a frequency range of 1 to 30 GHz. Klein and Swift (1977). The real part of the dielectric constant decreases steadily for higher frequencies and higher salinities. The imaginary part of the dielectric constant has a more non-linear relation with frequency and increases with salinity.

- pure water (Ulaby et al., 1986);

- saline water (Stogryn, 1971);

- saline water (Klein and Swift, 1977), for $f = 1.4$ to 30 GHz, best for $f < 10 GHz$;

- soil water adaptation of Stogryn (Dobson et al., 1985), for $f = 1.4$ to 18 GHz;

- soil water adaptation of Klein and Swift, for $f = 1.4$ to 18 GHz.

Klein and Swift is the most recent and will be used as the default. The dielectric models for the soil medium use the dielectric constant of soil water with a salinity of $sal_{soil} = 0$. The surface dielectric constant of the water tile is calculated using the saline water case with the salinity set to a constant value of $sal_{sea} = 32.5 psu$ for sea water ($LSM\,0.5$) and the value of sal_{soil} for small lakes and rivers.

In the case of sea ice, the dielectric constant is calculated according to Hallikainen (1995). When the soil temperature is below the freezing point, some or all off the soil water will be frozen and have the dielectric constant of ice. To account for this the dielectric constant of non-frozen soil is mixed with the dielectric constant of ice on the basis of soil temperature. The default fraction of frozen soil water is 0, for $T < -0.5C$

this is 0.5 and for $T < -5C$ the fraction is 1. Note that the L-MEB model used the variable 'frozen soil water content' to calculate the fraction of frozen versus non-frozen soil water.

3.1.3 Smooth Surface Reflectivity

The reflectivity of a flat surface r_s is given by the Fresnel law that defines the partition of electromagnetic energy at a dielectric boundary:

$$r_{sH}(\theta) = \left| \frac{\mu_s \cos(\theta) - \sqrt{\mu_s \varepsilon_{soil} - \sin^2(\theta)}}{\mu_s \cos(\theta) + \sqrt{\mu_s \varepsilon_{soil} - \sin^2(\theta)}} \right|^2 \tag{8}$$

$$r_{sV}(\theta) = \left| \frac{\varepsilon_{soil} \cos(\theta) - \sqrt{\mu_s \varepsilon_{soil} - \sin^2(\theta)}}{\varepsilon_{soil} \cos(\theta) + \sqrt{\mu_s \varepsilon_{soil} - \sin^2(\theta)}} \right|^2$$

where μ_s is the soil magnetic permeability, assumed to be unity. As soil moisture increases, ε_{soil} increases and the reflectivity increases. The Wilheit model (1978) calculates the r_s for a multi-layered soil, this is physically more correct but computationally more expensive. The layered approach makes it possible to use all the available profile data of temperature and soil moisture, without simplifying by means of the effective temperature. It is included for validation purposes only.

3.1.4 Roughness models

Because the natural land surface is generally not a specular reflector at microwave wavelengths r_s is corrected for roughness using one of the following models:

- Q/h model (Choudhury et al. (1979), Wang and Choudhurry (1981)), for $f = 1 - 10GHz$
  $h = (2k\sigma)^2$, with wavenumber $k[cm]$ and $\sigma[cm]$ the rms height of the surface

- Q/h model Wigneron et al. (2001), for $f = 1.4GHz$
  $h = 1.3972 \cdot (s/L_c)^{0.5879}$ with correlation length $L_c = 6cm$ and s $[cm]$ the standard deviation of surface height

- Q/h(VSM) model (Wigneron et al., 2001), for $f = 1.4GHz$
  $h = 0.5761(VSM)^{-0.3475} \cdot (s/xlc)^{0.4230}$

- Q/h(VSM,vegetation) model ATBD, for $f = 1.4GHz$

- ks horizontal emission based model (Wegmueller and Matzler, 1999), for $f = 1 - 100GHz$

Most of these models are based on Choudhury's Q/h formulation of roughness and polarization effects for microwave frequencies:

$$r_{r(P1)} = (Q \cdot r_{s(P2)} + (1-Q) \cdot r_{s(P1)}) \cdot exp(-h \cdot \cos^{Nrp}(\theta)) \tag{10}$$

(a) Roughness Height h

(b) Cross Polarization Q
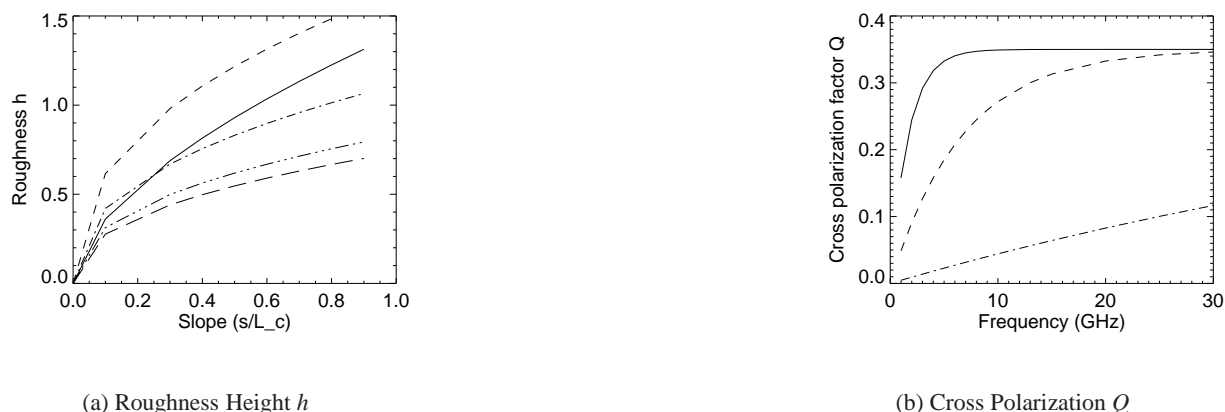
Figure 5: Roughness parameters: a) Roughness height h as a function of s/L_c according to Wigneron et al. (2001), solid line is not moisture dependant, the dashed lines are for 0.05, 0.15, 0.35 and 0.50 cm^3/cm^3 from top to bottom; and b) Cross polarization parameter Q as a function of frequency, for σ is 0.15, 0.5 and 1 cm.

where Q is the polarization mixing factor. Q can be considered zero at L-band Wigneron et al. (2001) and increases slightly with frequency: $Q = 0.35 \cdot (1.0 - exp(-0.6 \cdot \sigma^2 \cdot fghz))$ (Fig. 5). Only the roughness height h is changed in the various models. In ESA's Algorithm Theoretical Baseline Document (ATBD) on the operational soil moisture retrieval h is formulated as a function of soil moisture with vegetation dependant settings, this version is not yet fully implemented.

Wegmueller used a different approach to develop a semi-empirical model with a wide range of validity. In this model both horizontal and vertical polarized reflectivity is derived from the $r_s(H)$:

$$r_r(H) = r_s(H) \cdot exp(-1 \cdot (k \cdot \sigma)^{\sqrt{0.10 \cdot cos(\theta)}}) \tag{11}$$

For $(\theta <= 60): r_r(V) = r_r(H) \cdot cos(\theta)^{0.655}$ and for $(60 < \theta <= 70): r_r(V) = r_r(H) \cdot (0.635 - 0.0014 \cdot (\theta - 60))$.

For now, the Wigneron model will be used with roughness as a global constant.

3.2 Vegetation Component

The surface emission is attenuated by the vegetation and it acts as a source of emission itself (TB_{veg}). The attenuation is quantified by the atmospheric opacity τ_{veg} and is dependant on the vegetation characteristics, most importantly vegetation water content VWC. The following vegetation models are included:

- Effective Medium theory (Kirdiashev et al., 1979), for $f = 1\ to\ 7.5\ GHz$

- Geometrical Optics theory (Wegmueller et al., 1995), for $f = 1\ to\ 100\ GHz$

- b parameter approach (Wigneron et al., 1995), for $f = 1\ to\ 10\ GHz$

Vegetation water content has been derived from the ECOCLIMAP LAI data set (Masson et al. (2003)) following Pellarin et al. (2003):

$$VWC = 0.5 \times LAI \tag{12}$$

for grasslands and crops; the vegetation water content for rain forest, deciduous forests and coniferous forests has been set to 6, 4 and 3 kgm^{-2} (Pellarin et al. (2003), respectively. In Wigneron's model τ_{veg} is also related to the b parameter as defined in (Jackson and Schmugge, 1991). In both Kirdiashev's and Wegmueller's models the structure coefficient a_{geo} is used in the computation of τ_{veg}.

The low and high vegetation fraction, biome cover, dominant type and LAI are either obtained from ECO-CLIMAP (Masson et al., 2003) data or TESSEL (ECMWF) data. The ECOCLIMAP is a static vegetation dataset and contains monthly data for LAI and vegetation cover (crop cover is a function of LAI). The TESSEL dataset has no annual cycle in LAI (van den Hurk et al., 2000). The vegetation temperature is by default set equal to the surface temperature, but 2 m air temperature is also available as an option.

Water interception by the canopy after precipitation or dew can be very significant relative to the VWC. Potentially this effect can be accounted for by adding the interception reservoir to the low vegetation VWC. In the latest version of L-MEB the occurrence of high interception is flagged because interception data is considered too unreliable.

Since the annual trend VWC is important to our model, ECOCLIMAP will be the default data. In Section 5 the influence of the vegetation on the top-of-atmosphere brightness temperature is studied.

3.3 Snow Component

When snow is present, the land tiles are redistributed based on the snow cover fraction. The vegetation parameters are the same as for the tile with no snow and the calculation of the top-of-vegetation brightness temperature TB_{tov} is the same. For the tiles 'bare soil with snow' and 'low vegetation with snow' the snow is added as an extra layer above the vegetation. The effect of this extra layer on the TB_{tov} is calculated according to the HUT-snow emission model for a single snow layer (Pulliainen et al., 1999).

For the tile 'high vegetation with snow' only the snow on the surface is considered. The emission from the soil is computed with the effective temperature equal to the surface temperature. The extra snow layer is inserted and the emission above the snow layer is calculated according to Pulliainen et al. (1999). This snow corrected surface emission passes through the vegetation layer according to the vegetation component with the same values as for the high vegetation tile.

The snow cover is not analysed; for this study it is considered 100% if the snowdepth is greater than zero. The snow water content is set to $0.1[cm^3/cm^3]$ and the snow temperature is equal to the soil temperature of the first layer.

3.4 Atmospheric Component

The TB_{tov} is modified by the atmosphere before it reaches the satellite sensor. Attenuation of radiation is quantified by the atmospheric opacity τ_{atm}. Besides this, the atmosphere contributes through upward and downward emission parts TB_{au} and TB_{ad}. TB_{ad} contains the cosmic background radiation. The atmospheric variables can calculated using the following models:

- Profile approach after Liebe (2004);

- L-MEB, for $f = 1\ to\ 11\ GHz$;

- Lookup table Ulaby et al. (1986), for $f = 1\ to\ 90\ GHz$.

Table 1: Module choices for CMEM.

digitchoice.	0	1	2	3	4	5
1. Soil dielectric constant	-	Wang&Schmugge	Dobson	-	-	
2. T_{eff}	T_{surf}	Choudhury	Wigneron	Holmes	-	-
3. Reflectivity	-	Fresnel	Wilheit	-	-	-
4. Roughness	no	Choudhury	Wigneron1	Wigneron2	Wigneron3	Wegmueller
5. Vegetation	no	Kirdyashev	Wegmueller	Wigneron	-	-
6. Atmosphere	no	Pellarin	Liebe	Ulaby	-	-
7. T_{veg}	-	T_{surf}	T_{air}	T_{skin}	-	-
8. Veg Data	-	ECOCLIMAP	TESSEL	-	-	-

Similarly to the soil, the atmosphere is a medium with vastly fluctuating temperature and moisture profiles. Computation of the atmospheric factors considering atmospheric profiles of pressure, humidity, and temperature is described by Liebe (2004), this will only be used for validation of the simpler parameterizations.

For frequencies below 11 GHz, the vapor dependency can be disregarded and τ_{atm} can simply be related to the geopotential height at surface [m]. For frequencies above 11 GHz, accounting for water vapor density is required. A simple lookup table based on frequency of the τ_{atm} as a function of surface water vapor density is proposed by Ulaby et al. (1986).

3.5 Configuration of CMEM

The modular design of CMEM makes it possible to easily configure the model to the users specifications. There are two files that together define the model configuration; 1) the 'namelist' file which contains the model choices for each module and 2) the 'setup' file which contains the radiometric specifications, global constants and global parameters.

CMEM documents the module setup in the output filename in the form of an 8 digit code. The numbers in this code correspond to the eight most important configuration choices as shown in Table 1. All these modules have been discussed in the above sections. The zero option for a module means that a process is not modelled.

Table 2 summarizes the default set up of CMEM, L-MEB and LSMEM. In addition, values for the most important coefficients are given. Figure 6 shows an example of the synthetic brightness temperature at horizontal (a) and vertical polarization (b) for 1 July 2005 as computed using the CMEM standard set up. The range in temperatures from sea water, to ice and land areas is similar to what we find for C-band satellite data (e.g. AMSR-E).

(a) $TB_{toa[H]}$
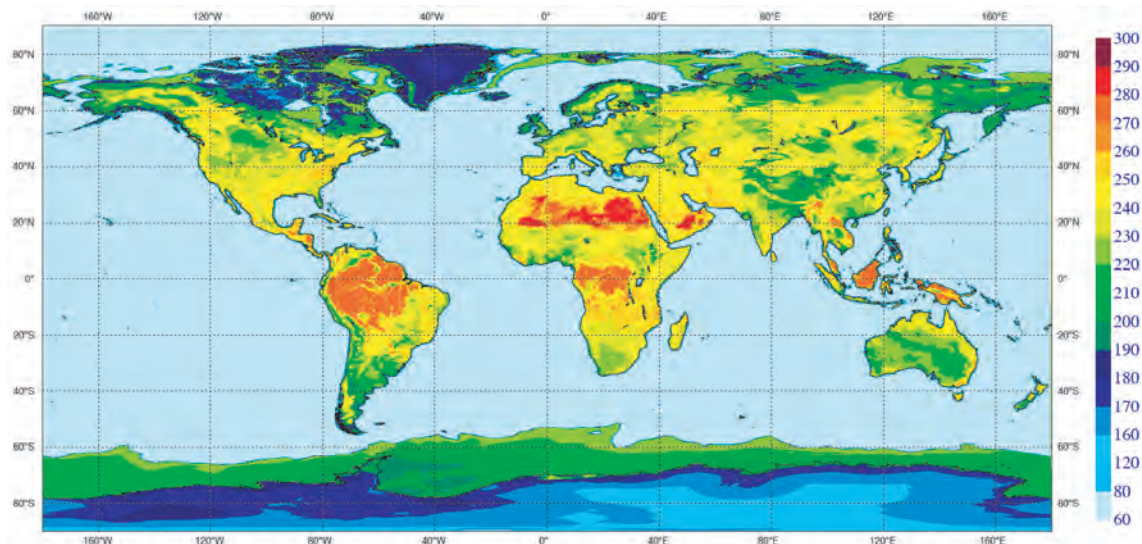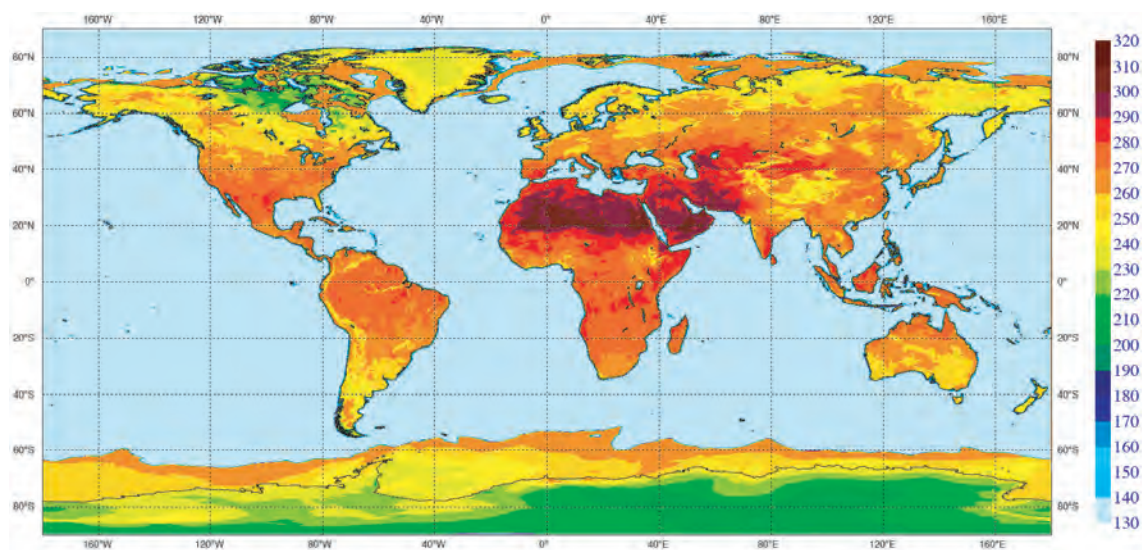
(b) $TB_{toa[V]}$

Figure 6: Brightness temperature, horizontal and vertical polarization at $\theta = 50^o$ for 1 July 2005, using the default CMEM setup.

Table 2: Model setup parameters for L-band.

		L-MEB	LSMEM	CMEM
Modules	Dielectric	Dobson	Dobson	Dobson
	T_{eff}	Wigneron	T_{surf} Wigneron	
	Reflectivity	Fresnel	Fresnel	Fresnel
	Roughness	Wigneron 1	Wegmueller	Wigneron 2
	Vegetation	Wigneron	Kirdyashev	Kirdyashev
	Atmosphere	Pellarin	Liebe	Pellarin
Input Data	Veg Data	ECOCLIMAP	TESSEL	ECOCLIMAP
	T_{veg}	T_{surf}	T_{air}	T_{surf}
Parameters	$sal_{soil}[psu]$	0	0.65	0
	$sal_{veg}[psu]$	6	6	6
	$sal_{sea}[psu]$	32.5	-	32.5
	$\sigma[cm]$	0.15	0.5	2.2
	$Q[-]$	0	f(sigma)	0
	$VWC[kg/m2]$	f(vegtype)	1.0/4.0	f(vegtype)
	$\omega[-]$	0.05/0.15	0.05	0.05
	$a_{geo}[-]$	(0.33,0.33)	(0.33,0.33)	(0.33,0.66)

4 Towards the assimilation of SMOS L-band brightness temperatures into numerical weather prediction models: A calibration / validation study based on ERA-40 re-analyses and Skylab observations

This section presents results on the calibration of CMEM using historic data and an initial quantification of systematic differences on the continental scale. Sections 4.2 and 4.3 summarize parts which have already been addressed earlier.

4.1 Skylab S-194 Observed Brightness Temperatures

Skylab was a polar-orbiting satellite mission covering the period from May 1973 to July 1977. It's nominal altitude was 435 km; the orbit period was 93 minutes. Among various remote sensing instruments was the S-194 passive microwave radiometer. This sensor was a nadir viewing L-band radiometer operating at 1.4 GHz (Jackson et al. (2004)). The resolution of a single observation is approximately 110 km, the distance between the centres of two consecutive footprints is 2.5 km.

Collecting data from S-194 required astronauts onboard the satellite. Consequently, the number of observations is limited to the following periods: 14 May - 22 June 1973, 28 June - 25 September 1973, and 16 November 1973 - 8 February 1974. The original S-194 data have never been archived. Jackson et al. (2004) recovered the observations used by Eagleman and Lin (1976); the data set and a comprehensive description are now available under *http://disc.gsfc.nasa.gov*.

In total, nine tracks of observations have been available (Fig. 1). Although the number of observations is quite limited it should be emphasised that a large variety of landscapes, vegetation types and climates is covered. Areas monitored by S-194 include the Rocky Mountains, the Central Great Plains, the Eastern US, and large

parts of the Amazon rain forests. In addition, the observation dates comprise several seasons including winter time observations. Consequently, this data set is useful to calibrate land surface emission models for global NWP applications.

4.2 ERA-40 Based Modelled Brightness Temperatures

The ERA-40 reanalysis data set (Uppala et al. (2005)) comprises the period from mid-1957 to 2001. The data sets used in the analysis comprise various satellite observations as well as ground based measurements and conventional synop data. These data sets were assimilated through the 3D-Var analysis scheme. The system made use of the Integrated Forecast System at T159 spectral resolution ($\sim 1.125^o$ horizontal spacing) with 60 vertical levels. The surface scheme within the IFS is the Tiled ECMWF Scheme for Surface Exchanges over Land (TESSEL) as described in van den Hurk et al. (2000). The soil is discretized in four layers of 0.07, 0.21, 0.72, and 1.89 m depths (from top to bottom). Vertical movement of water in the unsaturated zone is computed using the Richards equation and Darcy's law. Functional relationships between the hydraulic conductivity and diffusivity and soil water are specified according to Clapp and Hornberger (1978). Each grid box in the model is devided in up to eight tiles (bare ground, low and high vegetation without snow, exposed snow, snow under high vegetation, interception reservoir, ocean/lakes, and sea ice). The vegetation data base contains 20 different types, which are characterized by a set of fixed parameters. Although the surface is tiled, energy and water budgets are evaluated for a single atmospheric profile and soil profile per grid box. The archived fluxes for a grid box are area weighted-averages as derived from the individual tiles.

We used the Community Microwave Emission Model (CMEM) to solve the radiative transfer equations based on the ERA-40 reanalysis data set. The tiles used in CMEM are similar to the TESSEL tiles, but differ in that: 1) ocean, sea ice and lakes are all part of the water tile; 2) the interception reservoir, if at all modelled, is integrated in the vegetation water content and 3) snow on bare soil is treated as a seperate tile.

4.3 Auxiliary Data Sets and Initial CMEM Setup

For low frequencies the observed brightness temperature at the top of the atmosphere depends on a number of variables. Jones et al. (2004) ranked the main variables and parameters entering Eq. 1 according to their impact on TB_{toa}: Volumetric soil moisture, vegetation water content, soil roughness parameter, vegetation structure coefficient, effective soil temperature, vegetation single scattering albedo, soil bulk density, vegetation temperature, and soil texture. For this study, ERA-40 provides soil moisture fields (top 7 cm layer), soil temperature, snow depth, and 2 m temperatures as an approximation for vegetation temperature.

Vegetation water content has been derived from the ECOCLIMAP LAI data set (Masson et al. (2003)) following Pellarin et al. (2003):

$$VWC = 0.5LAI \tag{13}$$

for grasslands and crops; the vegetation water content for rain forest, deciduous forests and coniferous forests has been set to 6, 4 and 3 kgm^{-2} (Pellarin et al. (2003)), respectively for the first model calibration set up. The FAO soil texture data are static at 10 km spatial resolution and distinguish between 3 soil texture classes (coarse, medium, fine) (FAO (2000)). Sand and clay fractions have been computed from a look-up table according to Salgado (1999). The 10 km data sets have then been aggregated to T159 spectral resolution and the dielectric constant of wet soils has been computed following Dobson et al. (1985). The Dobson et al. (1985) model has been used previously in several L-MEB and LSMEM studies. It has to be noted that vegetation and soil parameters for the CMEM computations are not identical with the ones used for ERA-40. However, the operational

Table 3: Setup for Skylab studies.

Setup	Roughness	Vegetation	σ	$\omega(L,H)$	b (L,H)	$a_{geo}(L,H)$	$VW_{c(trop)}$
A	Wigneron Q/h	Wigneron	0.15	(0.05, 0.15)	(0.2, 0.33)		6
B	Wigneron Q/h	Wigneron	2.2	(0.05, 0.05)	(0.2, 0.33)		6
C	Wigneron Q/h(VSM)	Wigneron	2.2	(0.05, 0.05)	(0.2, 0.33)		6
D	Wigneron Q/h(VSM)	Kirdyashev	2.2	(0.05, 0.05)		(0.33, 0.33)	6
E	Wigneron Q/h(VSM)	Kirdyashev	2.2	(0.05, 0.05)		(0.33, 0.66)	10

forecast system at ECMWF will be revised within the next months to incorporate both vegetation and soil data sets. In addition, these auxiliary data sets will also be used in ESA's operational soil moisture retrieval.

Global data sets for soil roughness, vegetation structure coefficients, and vegetation single scattering albedo do not exist. In general, values have been derived from laboratory measurements or field experiments for a limited range of soil and vegetation types and specific parameterizations.

(1) *Soil roughness.* Physically based models generally depend on the characteristics of (measured) surface height profiles, namely the standard deviation of surface height σ and the correlation lengths L (Fung (1994)), and volumetric soil moisture. For large scale applications focussing on the retrieval / analysis of soil moisture simplified semi-empirical models are better suited. The majority of these simplified models uses a roughness height h and a polarization mixing parameter Q. Wigneron et al. (2001) developed two parameterizations for h as a function of (i) σ and L and (ii) σ and L and volumetric soil moisture. Both parameterizations are independent of incidence angle and polarization. This approach is well justified for the Skylab data analysed in this study; to make optimal use of the future multi-angular SMOS observations the parameterizations may have to be modified. For the first guess, values of 0.15 cm and 6.0 cm have been assigned for σ and L, respectively.

(2) *Vegetation structure coefficient.* Again, simplified semi-empirical models are used to characterize the influence of the vegetation on the observed brightness temperatures. Key parameters for the computation of the canopy opacity are the vegetation water content and the vegetation structure coefficient. In the 'classical' parameterization introduced by Kirdiashev et al. (1979) the vegetation structure coefficient a_{geo} includes the frequency, the dielectric constant of saline water, the density of water, and the incident angle. Other approaches (e.g. Jackson et al. (1999), Wigneron et al. (1995)) combine all these quantities in the so-called b-parameter. A compilation of b-parameter values from field experiments is available through Van de Griend and Wigneron (2004). For the initial computations the parameterization described in Wigneron et al. (1995) is used with b-parameter values of 0.2 and 0.33 for low and high vegetation, respectively. These are standard values, which have also been used in the global forward modelling study by Pellarin et al. (2003).

(3) *Vegetation single scattering albedo.* The single scattering albedo ω is defined as $\kappa_{sp}/(\kappa_{sp} + \kappa_{ap})$, with κ_{ap} the absorption coefficient and κ_{sp} the scattering coefficient. In various studies covering the frequency range from 1.4 to 37 GHz values from 0.03 to 0.127 were found (Kerr and Wigneron (1995)). For the first guess values of 0.05 and 0.15 have been used for low and high vegetation, respectively (Pellarin et al. (2003)).

The set up for the different CMEM runs described in the study are summarized in Tab.3. Model set up 'A' refers to the first guess set up as outlined in the preceding paragraphs. It mimics the L-MEB configuration as used in (Pellarin et al. (2003)).
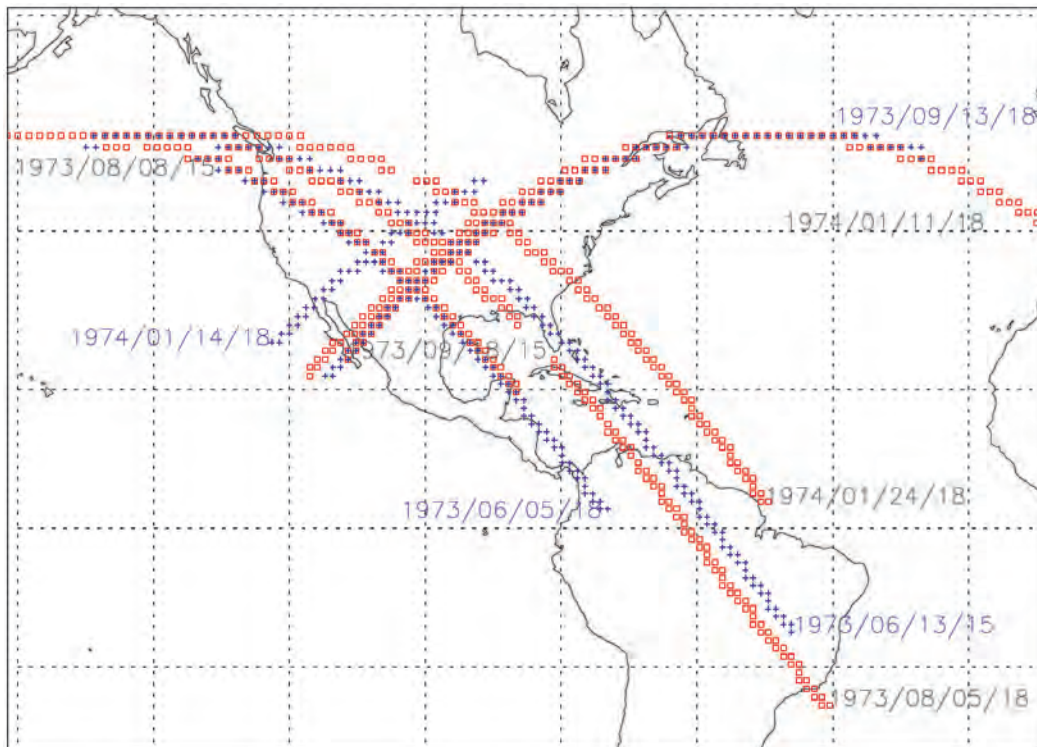
Figure 7: Spatial and temporal coverage of the Skylab S-194 observations. Blue tracks have been used for the calibration. The validation has been based on the red tracks.

4.4 Calibration Results

The spatial resolution and the sampling rate of the observations and the ERA-40 data set are different. Consequently, we averaged Skylab observation using the nearest neighbour technique to produce tracks of observed brightness temperatures at the ERA-40 grid. This is a reasonable approach since (i) the S-194 footprints are smaller than an ERA-40 grid box and (ii) brightness temperatures should be averaged rather than geophysical parameters to avoid errors introduced through non-linearities in the radiative transfer calculation (Drusch et al. (1999a), Drusch et al. (1999b)). Throughout the article these mean values have been compared. The variability of the observations within each ERA-40 grid box has been used to identify areas with a significant amount of open water bodies or coastal regions, which may not be treated correctly at T159 spectral resolution in the ERA data set. Whenever the minimum - maximum difference exceeded 10 K, the observation / model data pair has been rejected.

For the calibration part four tracks have been selected. They are shown in blue in Fig. 7 and cover North and South America and include winter and summer observations. The comparison between the initial set up 'A' as described in the previous paragraph and the observations is shown in Fig. 8 The spatial distribution of brightness temperature differences (observation - model) shows a good coverage of calibration data for North America. In South America, one transect including tropical forest has been obtained (Figs. 8a,b). The differences for North America can be as large as 40 K and in general, the modelled TB_{toa} are characterized by a low bias. The maps suggest that the differences over mountain areas and the Western US are generally larger than over the Central US. The scatter plots reveal a correlation of 0.66 and a bias of 19.4 K for the South America data (Fig. 8d). The data pairs over North America exhibit a correlation of 0.22 and a bias of 12.9 K.
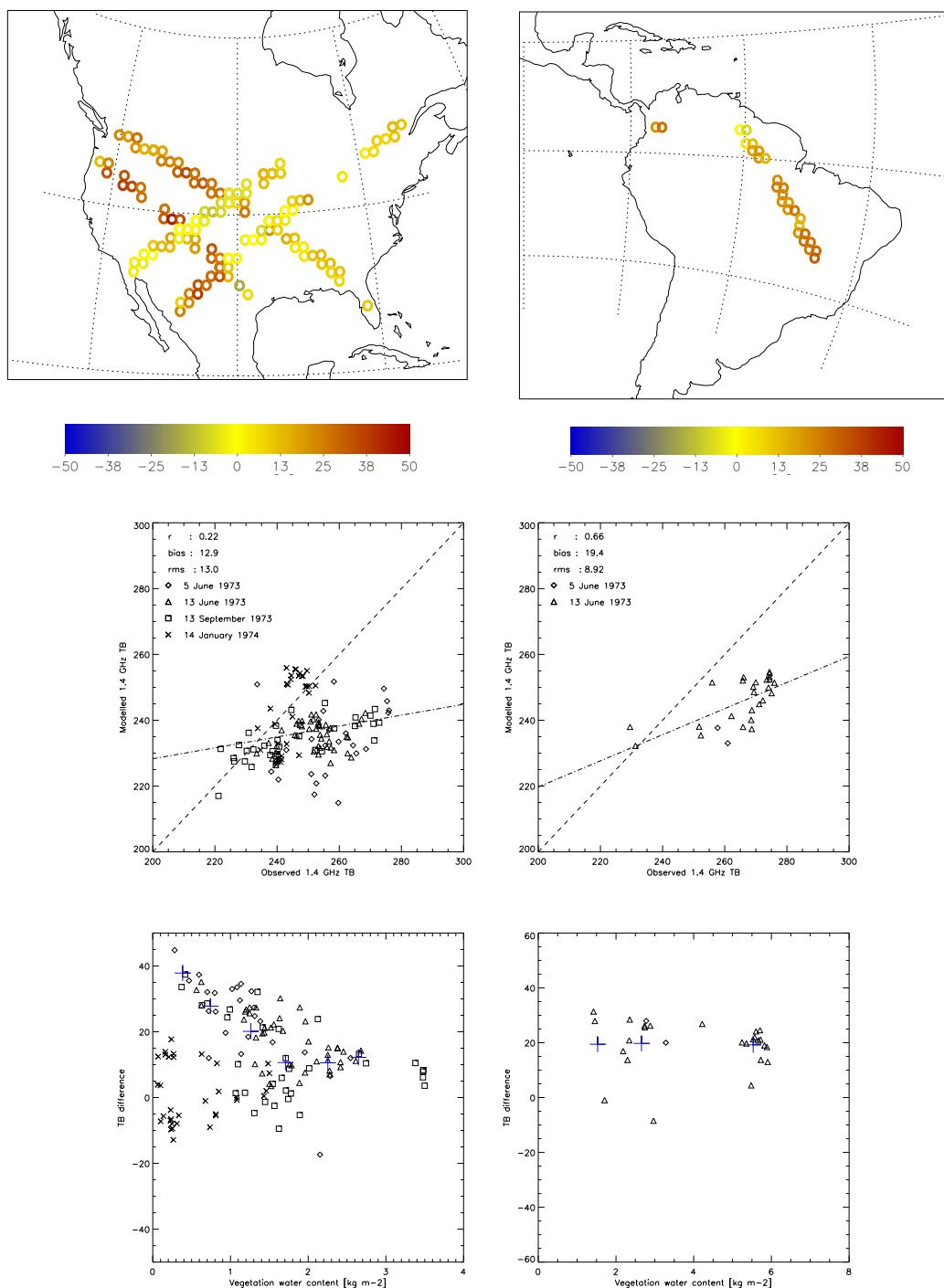
Figure 8: Comparisons between observed and modelled brightness temperatures (CMEM set up 'A'; Tab. 1): (1) Spatial distribution of observed TB - modelled TB (upper panel), (2) the corresponding scatterplots for North America (middle, left) and South America (middle, right), and (3) brigthness tempoerature differences as a function of vegetation water content (bottom panel). Blue crosses represent mean values for binned data.

The January 14 data are different in that they are almost bias free (Fig. 8c). This is somewhat surprising since large parts of the Western and Central US were snow covered during the overpass time and winter conditions are generally difficult to capture by emission models. However, Figs. 8a-d suggest a brightness temperature difference dependency on vegetation type. Among the various geophysical vegetation parameters the water content has the largest influence on the computed brightness temperatures. Figs. 8e,f show the the relationship between vegetation water content and brightness temperature difference. The blue 'plus'-signs indicate average values for binned data. For North America the data have been averaged for 0.5 kgm^{-2} intervals covering the range from 0 to 6 kgm^{-2}; the snow data from January 14 have been excluded since it can be assumed that most of the vegetation and the soil was snow-covered. For North America differences exceeding 40 K are obtained for sparsely vegetated areas. With increasing vegetation water content values decrease to $\sim$ 10 K. For the tropical forest in South America the differences between observed and modelled TB_{toa} are independent from vegetation water content at values around 20 K. These results point towards problems with the choice of the soil roughness, which is most prominent in sparsely vegetated areas, and the vegetation structure coefficient over regions with higher vegetation water contents.

To increase the modelled brightness temperatures the rms roughness height was increased to 2.2 cm. This value represents a medium-rough to rough surface and is supported through the field experiment described in Choudhury et al. (1979). With the correlation length L of 6 cm a a slope parameter of $\sigma/L = 0.36$ has been obtained. This is an average value, which is very well covered by observations used to derive the roughness parametrization by Wigneron et al. (2001). It translates into a roughness height h of 0.77. In addition, the single scattering albedo for high vegetation types has been reduced to 0.05. As already stated above, a global data set for the single scattering albedo does not exist. This modified model set up is summarized as 'B' in Tab. 3. The brightness temperature comparison for model set up 'B' is shown in Figs. 9a,b. The bias for North and South America data pairs has been reduced to -7.3 and -8.1 K respectively. The correlation between observations and model results is higher for North America and slightly lower for South America when compared against the results from model set up 'A'. As one would expect, the winter time observations from January 14 are least affected by the changes in roughness and vegetation. It is worth noting that the dynamic range in modelled brightness temperatures has hardly changed; the data show substantially less variability than the observations.

For model set up 'C' the modified parametrization for the computation of h including the soil moisture dependency has been selected (Wigneron et al. (2001)). For a σ/L ratio of 0.66, h values from $\sim$ 0.45 to $\sim$ 1.25 are obtained for soil moisture values of 35 and 3 %, respectively (Wigneron et al. (2001)). Again, the bias and rms errors over both continents is reduced (Figs. 9c,d). In addition, the dynamic range in the modelled brightness temperatures is slightly increased.

In the subsequent CMEM set ups the vegetation parameterization by Kirdiashev et al. (1979) has been used. For configuration 'D' a geometrical structure coefficient a of 0.33 has been assigned for low and high vegetation types (Fig. 9e,f). The North American data sets agree very well with a correlation coefficient of 0.6 and bias below 6 K. Over South America the modelled TB_{tao} are too low when compared against the corresponding observations. In configuration 'E' the vegetation water content for tropical forest has been increased to 10 kgm^2 and the structure coefficient a has been increased to 0.66 for high vegetation types. This value is more appropriate for stem dominated species (Wegmueller et al. (1995)). This set up is ideal since it yields acceptable biases over both continents. In addition, the dynamic range of the modelled values is comparably large (Figs. 9g,h).

The strong influence of the vegetation parametrization on the dynamic range of modelled brightness temperatures is somewhat surprising. In Fig. 10 TB_{toa} has been computed as a function of vegetation water content for high and low soil moisture values. The curves are 'nicht stetig' because of the change from low vegetation tile to high vegetation tile at a vegetation water content of 3 kgm^2. For low vegetation water contents both vegetation parameterizations result in a difference of $\sim$ 35 K.
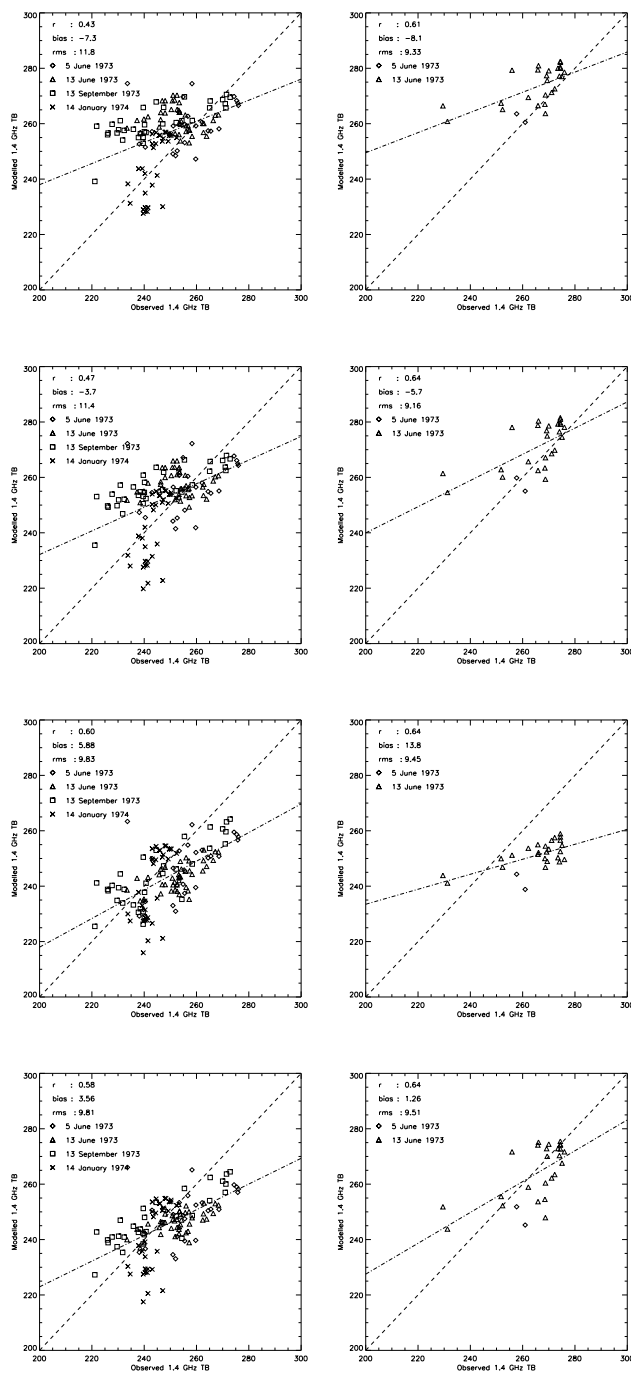
Figure 9: Differences between observed and modelled brightness temperatures for the CMEM set ups B to E (from bottom to top) as described in Tab. 3.
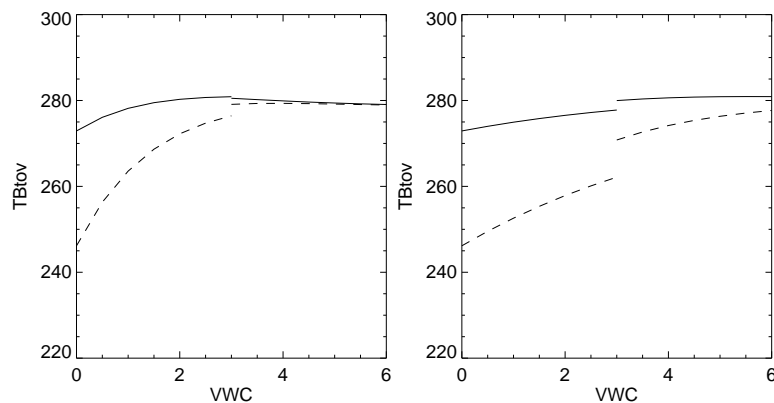
Figure 10: Sensitivity to VWC for the two vegetation models at L-band: (a) Wigneron et al. (2001), (b) Kirdiashev et al. (1979). Solid lines show the TB_{toa} for $VSM = 5\%$ and dashed lines for $VSM = 40\%$. The roughness height h is modelled following the soil moisture dependent Wigneron et al. (2001) model with a σ of 2.2 cm.

Using the Wigneron et al. (2001) model the vegetation becomes more and more opaque with increasing water content. For low vegetation tiles with 3 kgm^2 VWC a soil moisture difference of 35 % results in a brightness temperature difference of 5 K. Due to the lower fractional coverage of bare soil this difference is reduced to 1 K for high vegetation tiles (Fig. 10a). The Kirdiashev et al. (1979) formulation results in a more transparent vegetation layer. To get an opaque canopy VWC values of 10 kgm^2 are required.

4.5   Validation and Discussion

Observations from five overpasses have been used to validate CMEM set up 'E' (Fig. 1, red tracks). For North America the reference configuration 'A' results in systematic and random errors that are comparable to the values obtained for the calibration overpasses: the bias is 9.38 K and the rmse is 14.2 K. With configuration 'E' these values are reduced to 2.03 K and 11.4 K, respectively; the correlation coefficient is 0.67 (Fig. 5). Set up 'E' does not improve the modelled brightness temperatures for January 24. This particular overpass crosses the US from the northwest to the south east. This area is not well covered through the calibration data set and the parameters obtained from the calibration may not be appropriate.

Over South America the calibrated CMEM brightness temperatures compare very well with the observations. For the bias and the correlation coefficient values of -2.4 K and 0.75 have been obtained (Fig. 6). For three ERA-40 grid boxes over the Amazon region the modelled brightness temperatures are more than 16 K higher than the corresponding observations. The northern most data pair (Fig. 6a,b) showing a difference of 22 K includes the 'Serra da Mocidade' plateau and the 'Rio Branco', the footprint further to the south is strongly influenced by the 'Rio Negro' and the most southern data pair is located over an extended swamp area, the 'Ilha Tupinambarama'. It is likely that these complex terrains with a significant amount of open and vegetation covered water bodies are not represented correctly in the ERA-40 data set. If the data points were excluded from the analysis the values for correlation coefficient, bias, and rms were 0.83, -0.93 K, and 4.2 K, respectively.

Apart from the S-194 data used in this study, no spaceborne passive microwave L-band observations have been available on the continental scale. Parameterizations and coefficients for the land surface emissivity modelling have been derived form laboratory measurements and field experiments covering local to regional scales. This study demonstrates that it is possible to calibrate a state-of-the-art emission model for NWP data assimilation applications and for operational soil moisture retrievals. The results suggest that the proposed CMEM set up and its coupling to NWP model fields can be applied to a wide range of climates.

However, backward and forward radiative transfer modelling both depend on a number of auxiliary data sets and geophysical parameters, which are poorly known at large spatial scales. Each of these data sets has systematic and random errors. These (systematic) errors partly determine the value of a calibration parameter, e.g. the rms surface roughness height σ. Consequently, the values found in this study are not necessarily transferable to different NWP models; i.e. a land surface model with a different soil moisture climatology may need a different value for the roughness parameter. Following this rationale it is impossible to strictly validate individual parameterizations. The fact that the Kirdiashev et al. (1979) parameterization yields better results than the Wigneron et al. (2001) formulation could be an artefact of the NWP - CMEM coupling, the choice of the vegetation data set, or the definition of bare soil fraction for low and high tiles.

Although it is feasible to reduce the bias between the modelled brightness temperatures and the observations other systematic differences remain present. With the current NWP / CMEM set up it has not been possible to model the observed dynamic range of brightness temperatures. The observations seem to be characterized by higher spatial and temporal variabilities. This is a well known feature, which could be related to the difference in the vertical resolution of both data sets. Wilker et al. (2006) showed that for a given mean soil moisture value different vertical profiles in the top 7 cm layer could result in brightness temperature differences exceeding 5 K. However, these systematic differences should be minimized for the assimilation of brightness temperatures using Best Linear Unbiased Estimate (BLUE) techniques. Cumulative distribution function matching as proposed by Drusch et al. (2005) is one potential method.

This study addressed systematic differences between modelled brightness temperatures and the observations. As mentioned above these differences should be minimized for data assimilation applications to obtained statistically optimal analyses of soil moisture. The weight of the observations and the modelled first guess in the analysis is determined through their error characteristics. The rms errors obtained in this study include both, the first guess uncertainty and the observation error. Since the observations taken every 2 km along the flight path were averaged to represent an ERA-40 grid box it is very likely that the main contribution to the rms error values originates from the modelled brightness temperatures. For the ERA-40 soil moisture rms errors exceeding 4 % have been found when compared against in-situ observations over the US Southern Great Plains (Drusch et al. (2004)). A second major source of uncertainty is introduced through the vegetation data set. The ECOCLIMAP data represent an annual cycle but do not take inter-annual variability or variability on short time scales into account. A more detailed analysis on random errors will be needed once the SMOS observations are available.
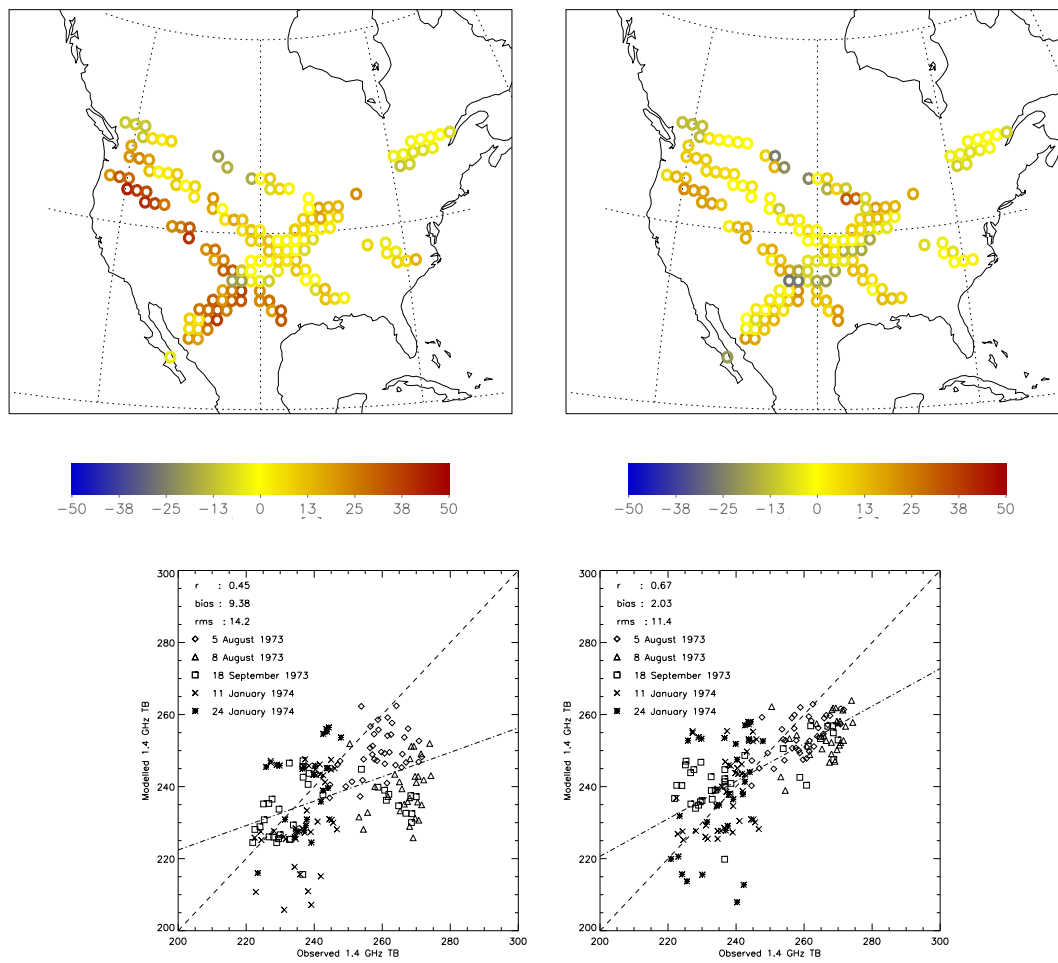
Figure 11:
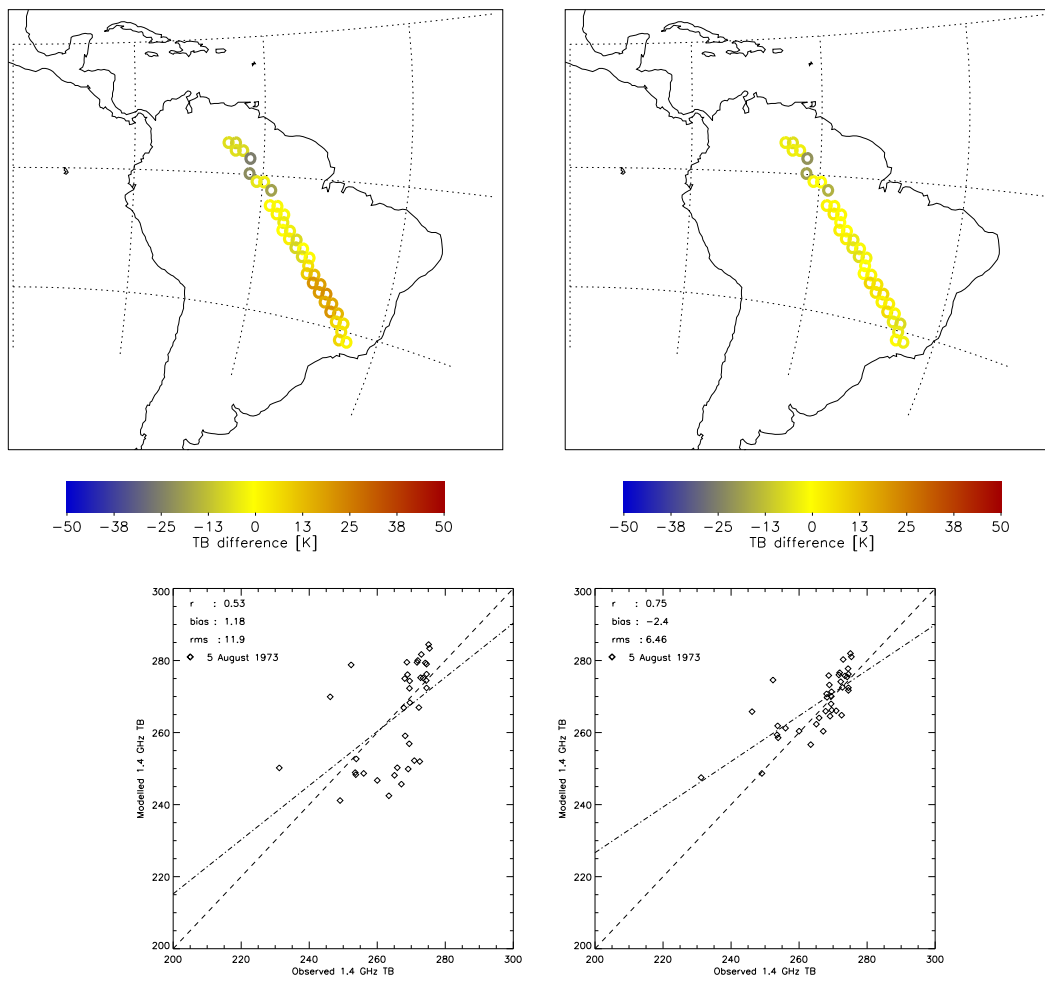
Figure 12:

5 Sensitivity to vegetation

The top-of-atmosphere brightness temperature is very sensitive to the presence of vegetation. CMEM relies on static input fields for the global distribution of vegetation characteristics and land cover. This makes it not only sensitive to the vegetation model, but also to the input data. Any calibration of the vegetation model will minimize the errors in the model and the vegetation database together. In this section we try to quantify the sensitivity to vegetation by: 1) comparing the difference in TB_{toa} as derived with ECOCLIMAP and TESSEL; and 2) see how this difference is influenced by the choice of vegetation model.

5.1 Materials and Methods

The CMEM model makes use of a static vegetation database to quantify the radiative properties of the vegetation in each cell. For each land cell this database includes: low and high vegetation fraction, biome cover, dominant vegetation type and LAI. Vegetation water content is related to LAI for low vegetation and for high vegetation a constant value is assigned depending on vegetation type. The current implementation of CMEM makes it possible to switch between two different vegetation databases.

The first database is the one used in the ECMWF TESSEL surface scheme (van den Hurk et al., 2000). The TESSEL database contains 20 vegetation types with fixed values for all the vegetation characteristics. This means there is no annual cycle in LAI, nor in biome cover. The second available vegetation database is ECO-CLIMAP (Masson et al., 2003) . This is the newest of the two vegetation databases and has 215 ecosystem types based on a combination of existing land-cover and climate maps with satellite data. In ECOCLIMAP there are for each ecosystem monthly estimates of LAI. Biome cover (BC) is a constant 95% or 99% for all ecosystems, with the notable exception of crops where it is related to LAI ($BC = 1 - EXP(-0.6 \cdot LAI)$) and therefore changes through the year.

Besides the input of vegetation characteristics there are also three different vegetation models coded in CMEM to calculate the vegetation opacity (See section 3.2). They contain the Effective Medium theory (Kirdiashev et al., 1979), Geometrical Optics theory (Wegmueller et al., 1995), and the b parameter approach (Wigneron et al., 1995). All these models relate τ_{veg} primarily to VWC, but have different sensitivities. The choice of vegetation model will have influence on the quantitative difference between the two vegetation databases.

5.2 Results

To test the sensitivity of CMEM to the vegetation input, we look at the difference in the modelled ΔTB_{toa} when the vegetation database is changed from ECOCLIMAP to TESSEL. Figure 13 shows the ΔTB_{toa} for the first day of every month in 2005.

The differences mainly vary between +10 and -10 K, but some regions show a much higher permanent difference (see for example in South America, South Africa). In the northern hemisphere, the ECOCLIMAP values are up to 20 K lower in the winter and up to 10 K higher in the summer. This annual cycle can be fully attributed to the annual cycle in the LAI and crop cover in ECOCLIMAP. The microwave emission is highly sensitive to vegetation water content that changes with LAI for low vegetation. The difference will therefore change through the year as the LAI changes in ECOCLIMAP and stays constant in TESSEL.

When these monthly figures are averaged over the year the δTB_{toa} is somewhat lower but still very significant (see Figure 14). The differences due to changing LAI are removed, but the regions with a permanently high difference are not affected. Maximum differences can reach 20 K. For example, ECOCLIMAP has much

higher cover fractions of high vegetation then TESSEL in Portugal, New Zealand and parts of Siberia leading to ΔTB_{toa} of $+15K$. On the other hand ECOCLIMAP has much lower high vegetation coverage in Ireland and the Southern coast of West-Africa which results in ΔTB_{toa} of $-20K$. On the whole, ECOCLIMAP underestimates TB_{toa} by -4 K relative to TESSEL.

This strong vegetation effect can be explained by the high sensitivity of the vegetation models to the VWC of low vegetation water content (Figure 16). According to the Kirdiashev model, a change of $1kg/cm^3$ in vegetation water content results in 5 K difference in brightness temperature. For the Wigneron model in its current configuration this effect would be double as strong. Besides different estimates of LAI for low vegetation, the difference in cover of low vegetation, high vegetation and bare soil will make differences in tile averaged VWC of several LAI points very likely. Figure 15 shows the difference in VWC for December.

5.3 Conclusion

This study of the effect of changing the vegetation input database shows that the representation of vegetation in the radiative transfer model is a first order effect with differences in L-band brightness temperatures of 5-10 %. It clearly shows that using a static vegetation database to represent the vegetation layer in an emission model places large presumptions on the interpretation of observed brightness temperatures. This means that if the amount of vegetation is overestimated in the vegetation database, the emission model will have to be calibrated to underestimate the effect of vegetation on brightness temperatures, and vice versa. This will make the calibrated model higly linked to the vegetation database that is used. Changing the database will need to be followed by recalibrating the model.

Another result of a predefined vegetation database is that all deviations in actual vegetation will be recorded in the soil moisture variable. For example, if in a certain region spring comes exceptionally late, the vegetation database will overestimate the vegetation compared to the the actual vegetation. The model will then underestimate the effect of soil moisture and the retrieved soil moisture value will then be too high.
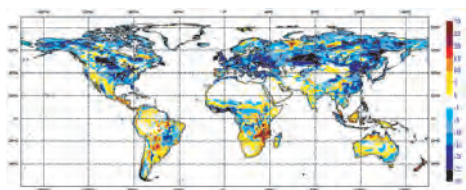
(a) January
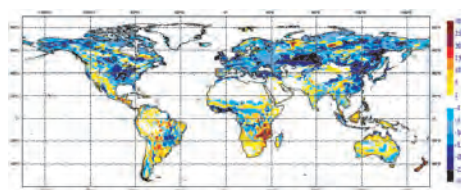
(b) February
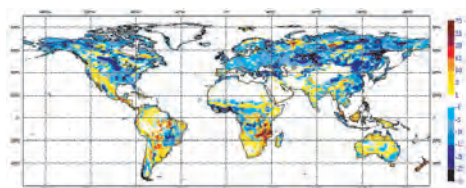
(c) March
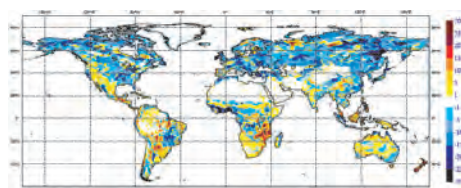
(d) April
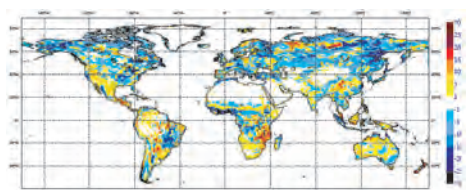
(e) May
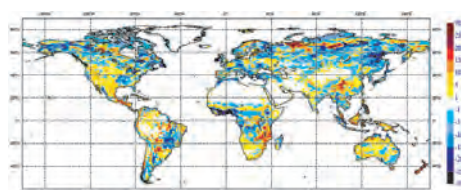
(f) June
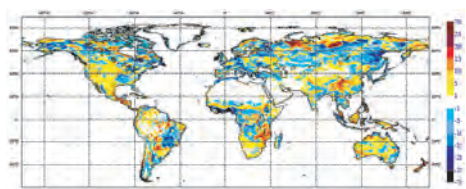
(g) July
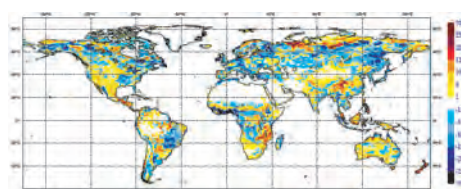
(h) August
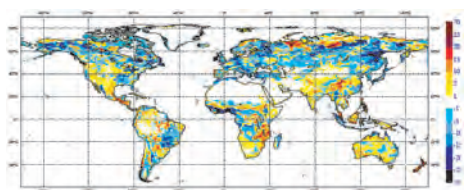
(i) September
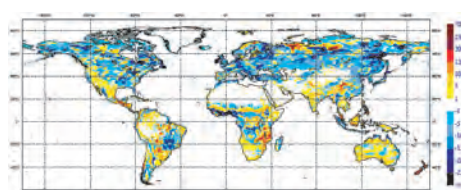
(j) October
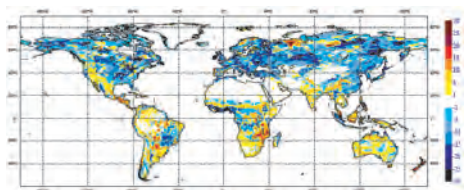
(k) November
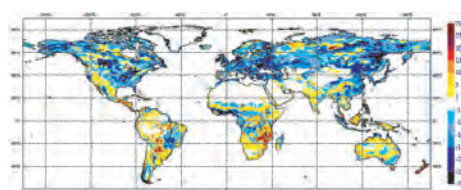
(l) December

Figure 13: Brightness temperature [H], vegetation ECOCLIMAP - ECMWF
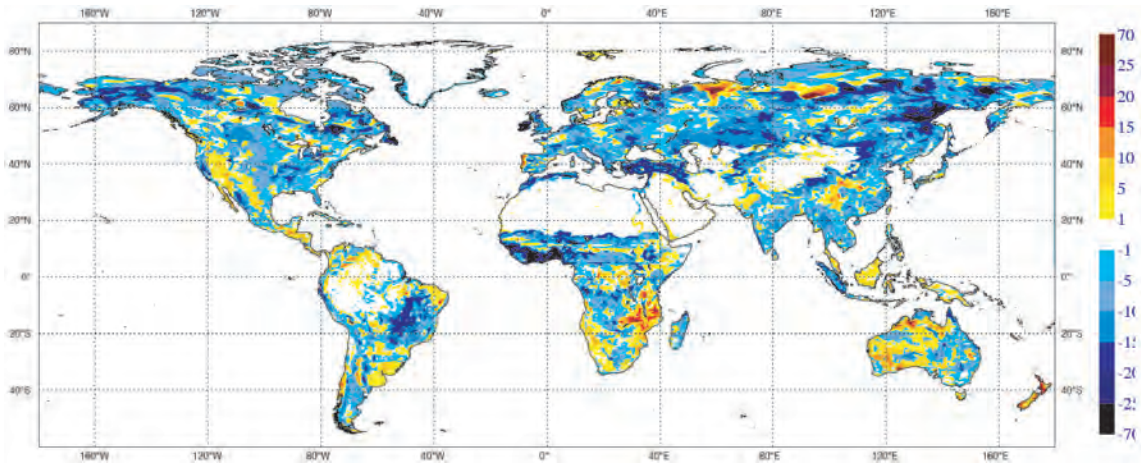
(a) Wigneron (A) $Avg = -3.9K$
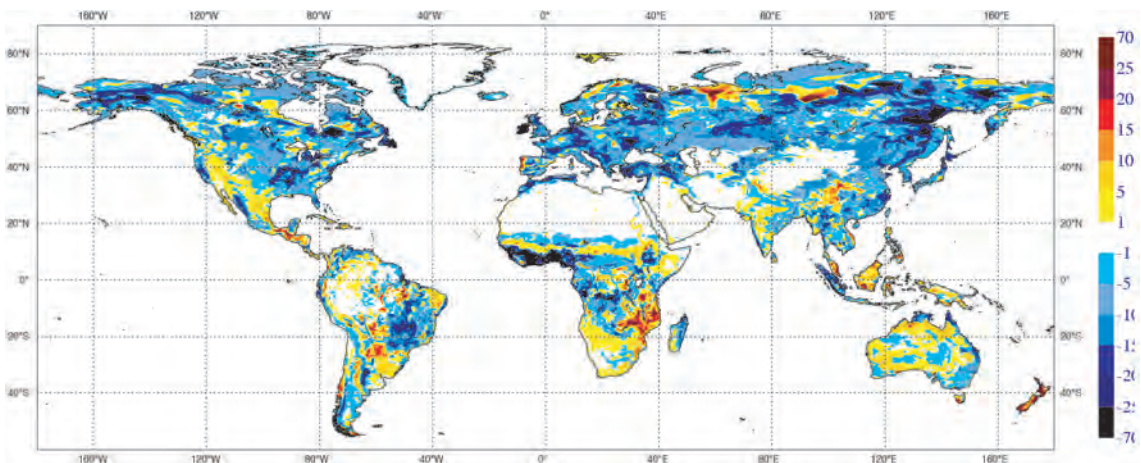
(b) Kirdyashev (E) $Avg = -4.0K$

Figure 14: Mean difference in $TB_{(H.f=1.4GHz)}$, ECOCLIMAP - TESSEL, for day 1 of every month of 2005. The vegetation model is a) Wigneron; b) Kirdyashev.
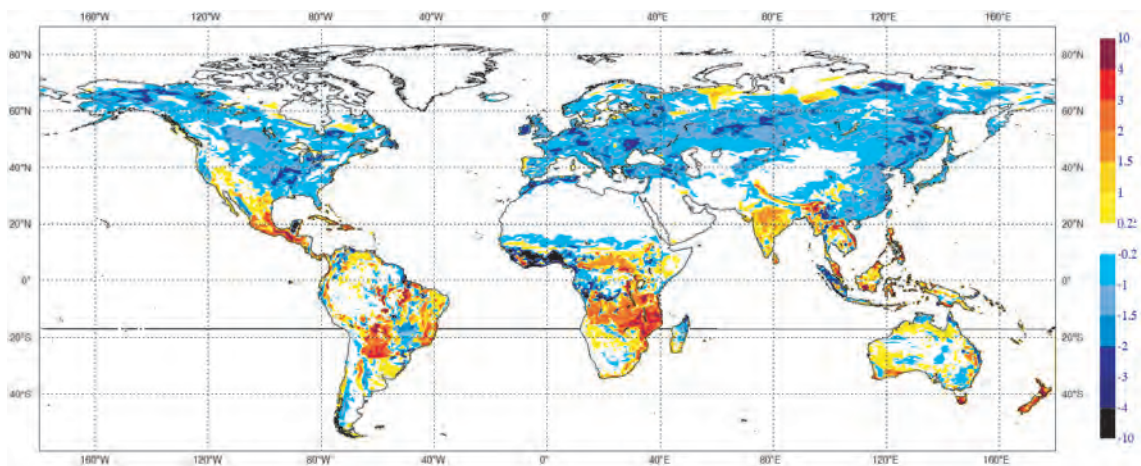

Figure 15: Mean difference in VWC, ECOCLIMAP - TESSEL, for December.

(a) Wigneron   (b) Kirdyashev   (c) Wegmueller
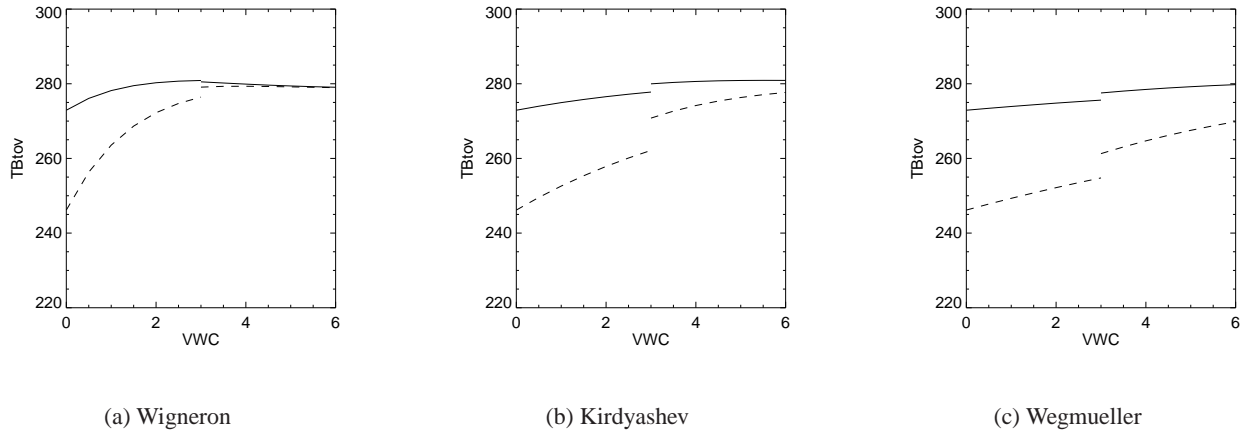
Figure 16: Sensitivity to VWC for the three vegetation models at L-band. Solid lines show the TB_{tov} for $VSM = 0.05$ and dashed lines for $VSM = 0.40$. The roughness height h is modelled following the Q/h(VSM) model (Wigneron et al., 2001) with an σ of 2.2 cm. At low moisture values, the three models are relatively insensitive to vegetation, but at high moisture the difference between TB_{soil} and TB_{veg} increases making them very sensitive to VWC. Wigneron's vegetation model is in this configuration the most sensitive and saturates at lowest VWC value.

6 Sensitivity analysis using an Ensemble Prediction System

The atmosphere is a complex dynamical system with many degrees of freedom. In numerical weather prediction (NWP), the state of the atmosphere is described by the spatial distribution of wind, temperature, specific humidity, liquid water content and surface pressure. The mathematical differential equations used to predict the system time evolution include Newton's laws of motion and the laws of thermodynamics. Numerical weather prediction models predict the time evolution of the atmospheric state by solving numerically the system equations.

A deterministic forecast is a single integration of the system equations. The practical usefulness of a single deterministic weather forecast is limited by the day-to-day variability in its accuracy. This variability is partly associated with fluctuations in the predictability of the atmospheric flow, with predictable states (i.e. flows characterized by a slow amplification of initial errors) alternated by unpredictable states (i.e. flows characterized by a fast amplification of initial errors).

Ensemble systems are practical tools designed to assess the predictability of the daily atmospheric flow (ref: Encyclopedia of Atmospheric Sciences, Academic Press, 2002, in press). More generally, they can be used to predict the time evolution of the probability density function (PDF) of forecast states. Ensemble systems should be designed to simulate the effect of all sources of forecast errors. In particular, they should simulate the effect of uncertainties in the knowledge of the initial state of the system and the effects of the approximations made in numerical weather prediction models.

6.1 Materials and Methods

The ECMWF Ensemble Prediction System (EPS) is one of the most successful global ensemble prediction systems run on a daily basis **?**. In this study, we look at the 48 hour forecast of ECMWF TL159C31 EPS with 50 perturbed members (Buizz et al. 1998). After 48 hours, the surface state in the 50 members will exhibit a low variance in areas with high predictability and a high variance in areas where the predictability is low.

Hereunder, the variance in soil moisture after 48 hours will be used as an indicator of the uncertainty in the initial conditions for deterministic weather forecasting.

In order to identify the regions with highest potential for assimilation of satellite derived soil moisture we use CMEM to model the top-of-atmosphere L-band brightness temperature (TB_{toa}) based on the 48 hours prediction for each of the 50 members of the EPS. This is done for day 1 and 15 of every month of 2005 to get a representative average of the weather conditions. At a specific location, a high variance in soil moisture and or temperature will result in a high variance in TB_{toa} if the model is sensitive to the surface state at that location. The most important factor that has a negative effect on the soil moisture sensitivity of the model at a certain location is the presence of vegetation. Vegetation can already saturate the microwave emissivity at VWc levels of 3 to 4 kg/cm^3 (recall Figure 16). Another factor can be a high percentage of open water in a grid box which will decreases the dynamic range in emissivities. Factors that can increase the sensitivity of the model relative to the variance in soil moisture and temperature are temperatures around the freezing point and intermittent snow events.

Taken together, the variance in TB_{toa} as based on the 50 members of the EPS will thus be a qualitative indicator of regions where both the uncertainty in initial conditions is high and the sensitivity of a satellite-borne L-band radiometer to soil moisture will be high. Figure 17 shows the variance in predicted TB_{toa} on the left, and the variance in VSM on the right, for the first day of every month of 2005. This shows that for most regions, a high variance in soil moisture will result in a high variance in TB_{toa}, see for example Australia in January. In other regions (e.g. the Amazon, central Africa.) a variance in soil moisture has little effect on the predicted TB_{toa}. The different sensitivity to soil moisture can in this case be explained by a different vegetation density. The effect of open water in a grid box is difficult to separate from that of vegetation density because they often occur together. Relatively high variances in TB_{toa} as compared to the variance in VSM can be seen in northern latitudes, see for example Canada in November and December. This can likely be attributed to temperatures around the freezing point and snow cover.

6.2 Results and Conclusion

The average of the 24 variance maps is shown in Figure 19 for $TB_{toa,H}$ (top figure) and VSM (bottom figure). The map of the average variance in VSM is very evenly filled with a variance of 1-2 % (except for deserts) and shows that the sample size is big enough to reduce the impact of one-time events. The map of the variance in $TB_{toa,H}$ shows now clearly the regions where both the initial conditions in NWP are the most uncertain and L-band microwave data have a high sensitivity to soil moisture. According to this map these regions are between 30 and 60 degrees Northing in both America and Eurasia, in Australia, South Africa and the southern tip of South America

This study gives valuable information on potential use for satellite measurements of L-band microwave emission. It identifies regions where a high sensitivity of L-band emission to soil moisture combines with uncertainty in initial conditions in numerical weather prediction. Figure 20 shows a scatter plot of variance in VSM versus TB_{toa}, with hypothetical regressions for dense forest ($0.2K/\%$), low vegetation ($1K/\%$) and bare soil ($2K/\%$). Further studies should test these hypothesis and seek to isolate different biomes and their potential for passive microwave remote sensing. Also, the effect of frozen soil and snow should be separated from the analysis because the TB_{toa} is not likely to give good information.
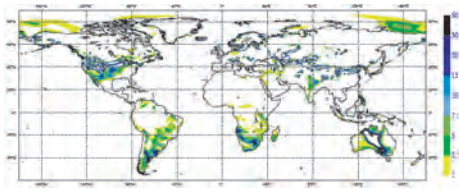
(a) TB_H January
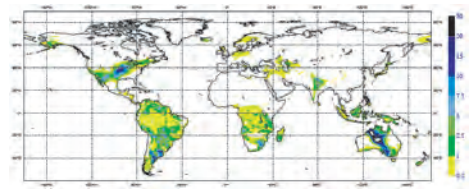
(b) VSM January
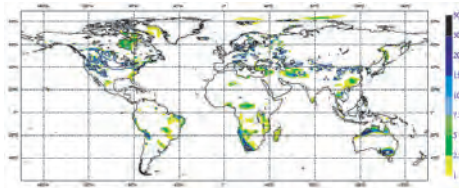
(c) TB_H February
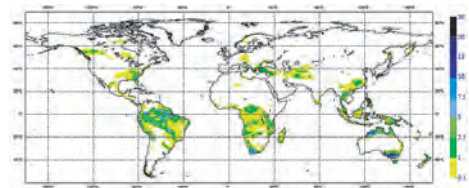
(d) VSM February
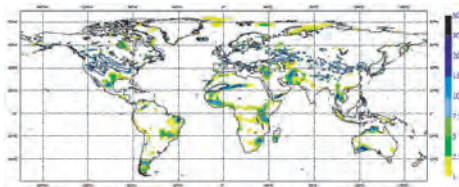
(e) TB_H March
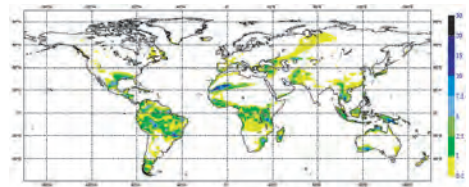
(f) VSM March
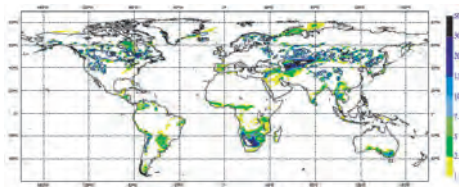
(g) TB_H April
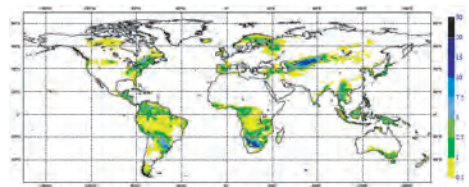
(h) VSM April
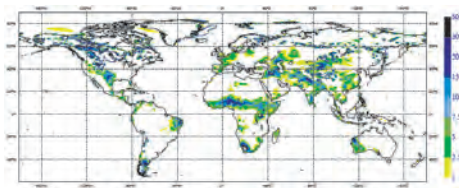
(i) TB_H May
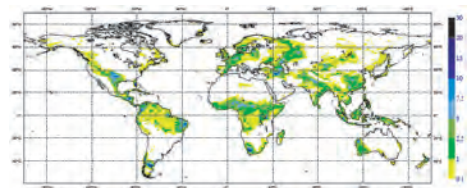
(j) VSM May
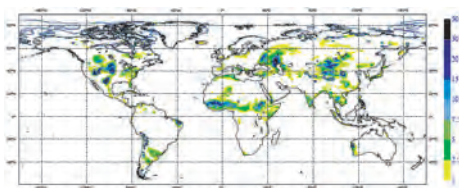
(k) TB_H June
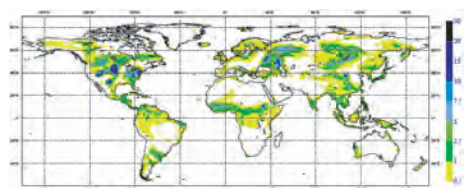
(l) VSM June

Figure 17: Variance in Tb[H] (left panel) and VSM (right panel) of day 1 for first six months of 2005 at 12PM.
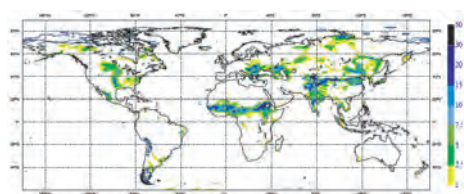
(a) TB_H July
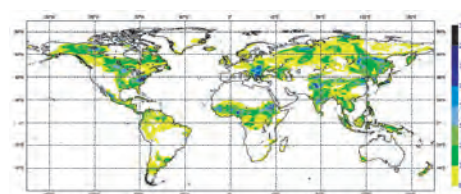
(b) VSM July
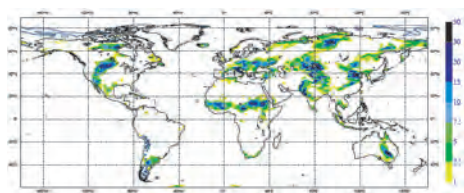
(c) TB_H August
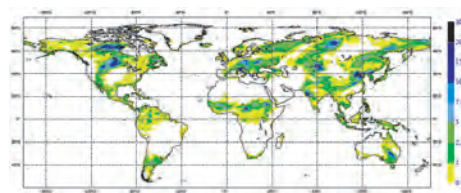
(d) VSM August
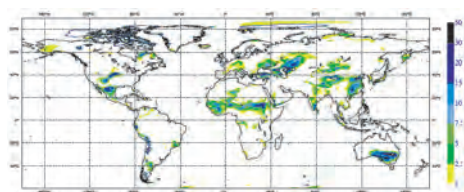
(e) TB_H September
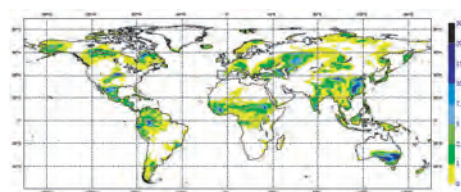
(f) VSM September
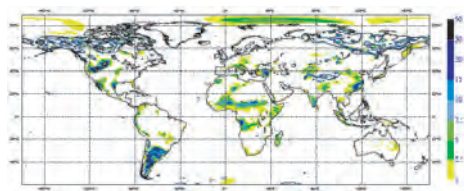
(g) TB_H October
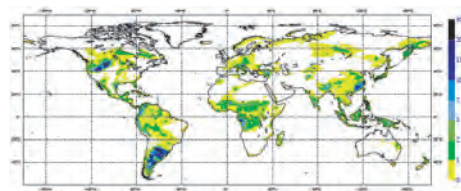
(h) VSM October
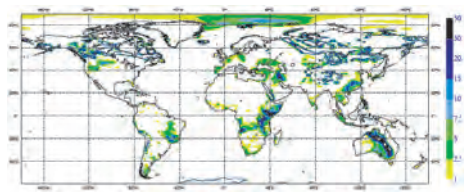
(i) TB_H November
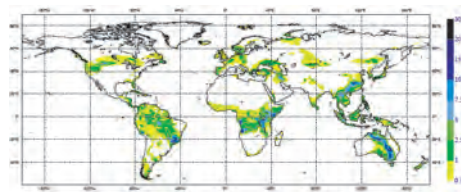
(j) VSM November
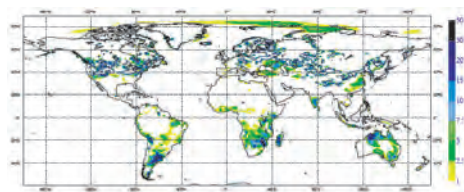
(k) TB_H December
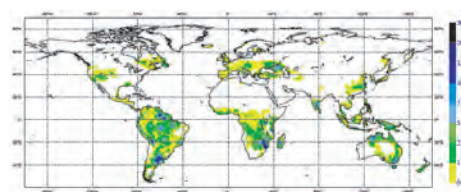
(l) VSM December

Figure 18: Variance in $TB[H]$ (left) and VSM (right) of day 1 for second half of 2005 at 12PM.
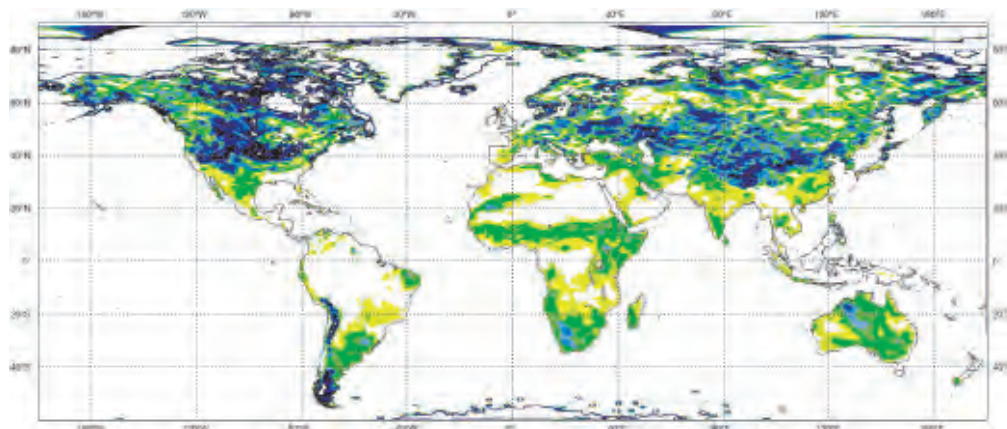
(a) $Tb[H]$
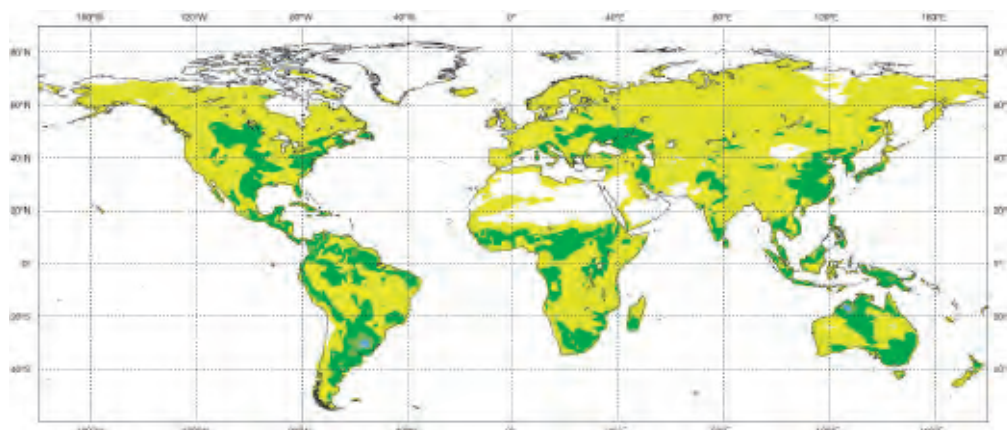
(b) VSM

Figure 19: Mean of the variances in $Tb[H]$ and VSM of day 1 and 15 for every month of 2005 at 12PM.
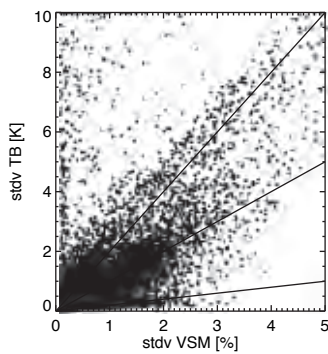
Figure 20: Standard deviation in VWC against Standard deviation in $Tb[H]$ for January.

7 Future work

7.1 Calibration on RTTOV surface emissivities

The Radiative Transfer for TOV (RTTOV) is used by the ECMWF to assimilate passive infrared and microwave radiances from satellites in the numerical weather prediction model. Using an advanced atmospheric model, the emissivity of the single layer soil-vegetation surface can be derived. A model like CMEM makes it possible to compare the observed emissivities to the predicted emissivities according to a soil model consistent with the ECMWF surface fields. Theoretically, the observed emissivity from RTTOV e_o compares to the modelled CMEM emissivity e_m in the following way:

$$TB = TB_{au} + T_{skin} \cdot e_o \cdot exp(-\tau_a) + TB_{ad} \cdot (1 - e_o) \cdot exp(-\tau_a) \tag{14}$$

$$e_o = ((TB - TB_{au})/exp(-\tau_a) - TB_{ad})/(T_{skin} - TB_{ad}) \tag{15}$$

Because RTTOV treats the land and vegetation as a single layer, the e_o can not simply be related to the modelled TB_{tov} because the TB_{ad} gets attenuated twice by the vegetation. Therefore the TB_{tov} as calculated from CMEM without atmosphere can be compare to e_o in the following way:

$$e_o = \frac{TB_{tov}}{T_{skin}} - \frac{TB_{ad} \cdot (1 - exp(-2\tau_{veg}))}{T_{skin}} \tag{16}$$

Correcting for TB_{ad} needs a slightly more complicated approach. For a first estimate we will look at C- and X-band data of AMSR-E where the effect of TB_{ad} will be less then 1%.

7.2 Open issues

- Global distribution of roughness effects;

- Calibrate the effective temperature models on the Wilheit model, average over different months;

- Water tile has constant salinity of $32.5psu$ for oceans and great lakes (LSM¿0.5) else $0.0psu$ for fresh water. For coasts, water in sea and water in lakes have the same salinity. Lake Cover (CL 26) is not archived in MARS;

- Water interception by canopy is not included in the model. Make it possible to flag the data or include it in low vegetation water content as in L-MEB.

- Amount of frozen water in soil is poorly defined. (frostfrac in soil module); Pellarin uses $/tau$ threshold for different vegetation densities

- Snow module, Water content snow as input field and snow cover as function of snow depth;

Acknowledgements

References

Balsamo, G., J.-F. Mahfouf, S. Bélair, and G. Deblonde (2006), A global root-zone soil moisture analysis using simulated L-band brightness temperature in preparation for the HYDROS satellite mission, *accepted by J. Hydromet.*.

Buiza, R. (2002), Encyclopaedia of Atmospheric Sciences, Academic Press, *in press*.

Buiza, R. (2006), The ECMWF Ensemble Prediction System, Chapter 17 of 'Predictability of Weather and Climate', *publisher: Cambridge University Press*, 459–489..

Drusch, M., E. Wood, and H. Gao (2006), Initializing numerical weather prediction models with satellite de-rived surface soil moisture: Data assimilation experiments with ECMWF's Integrated Forecast System and the TMI soil moisture data set, *accepted by J. Geophys. Res.*

Drusch, M., E. Wood, and H. Gao (2005), Observation operators for the direct assimilation of TRMM Mi-crowave Imager retrieved soil moisture, *Geophys. Res. Let.*, *32*, L19503, doi:10.1029/2005GL023623.

Drusch, M., E. Wood, H. Gao, and A. Thiele (2004), Soil moisture retrieval during the Southern Great Plains hydrology experiment 1999: A comparison between experimental remote sensing data and operational prod-ucts, *Wat. Res. Res.*, *40*, W0250410, doi:10.1029/2003WR002441.

Drusch, M., E. Wood, and T. Jackson (2001), Vegetative and atmospheric corrections for soil moisture retrieval from passive microwave remote sensing data: Results from the Southern Great Plains Hydrology Experiment 1997, *J. Hydromet.*, *2*, 181–192.

Gao, H., E. Wood, T. Jackson, M. Drusch, and R. Bindlish (2006), Using TRMM/TMI to retrieve soil moisture over the southern United States from 1998 to 2002, *J. Hydromet.*, *7*, 23–38.

Gao, H., E. Wood, M. Drusch, W. Crow, and T. Jackson (2004), Using a microwave emission model to estimate soil moisture from ESTAR observations during SGP99, *J. Hydromet.*, *5*, 49–63.

M. C. Dobson, F. T. Ulaby, M. T. Hallikainen, and M. A. El-Rayes. Microwave Dielectric behavior of wet soil - part II: Dielectric mixing models. *IEEE Trans. Geos. Remot. Sens*, 23(1):35–46, 1985.

Drusch, M., E. Wood, and R. Lindau (1999b), The impact of the SSM/I antenna gain function on land surface parameter retrieval, *Geophys. Res. Let.*, *26*, 3481–3484.

Drusch, M., E. Wood, and C. Simmer (1999a), Up-scaling effects in passive microwave remote sensing: ESTAR 1.4 GHz measurements during SGP97, *Geophys. Res. Let.*, *26*, 879–882.

Eagleman, J.R. and W.C. Lin (1976), Remote sensing of soil moisture by a 21-cm passive radiometer, *J. Geo-phys. Res.*, *81*, 3660–3666.

FAO (2000), Digital Soil Map of the World and Derived Soil Properties. Rev. 1. (CD Rom), 1, FAO Land and Water Digital Media Series. *available under http://www.fao.org/ag/agl/agll/dsmw.htm*

Fung, A.K. (1994), Microwave scattering and emission models and their applications, *Norwood, MA: Artech House*

Holmes, T.H. and M. Drusch (2007), The SMOS Community Microwave Emission Model (CMEM), *ECMWF Technical Memorandum*, *???*, ?? pages.

Jackson, T.J., D.M. LeVine, A.Y. Hsu, A. Oldak, P.J. Starks, C.T. Swift, J.D. Isham, and M. Haken (1999), Soil moisture mapping at regional scales using microwave radiometry: The Southern Great Plains Hydrology Experiment, *IEEE Trans. Geo. Rem. Sens.*, *37*, 2136–2151.

Jackson, T.J., A.Y. Hsu, A. Van de Griend, and J.R. Eagleman (2004), Skylab L-band microwave radiometer observations of soil moisture revisited, *Int. J. Rem. Sens.*, *25*, 2585–2606.

Jones, A.S., T. Vukicevic, and T.H. Vonder Haar (2004), A microwave satellite observational operator for variational data assimilation of soil moisture, *J. Hydromet.*, *5*, 213–229.

Kerr, Y.H. and J.P. Wigneron (1995), *Vegetation models and observations - a review*, in Passive Microwave Remote Sensing of Land-Atmosphere Interactions, Eds. B.J. Choudhury, Y.H. Kerr, E.G. Njoku and P.Pampaloni, VSP Utrecht, NL, 685 pp.

Masson, V., J.-L. Champeaux, F. Chauvin, C. Meriguet, and R. Lacaze (2003), Soil moisture retrieval from AMSR-E, *J. Climate*, *16*, 1261–1282.

Njoku, E.G., T.J. Jackson, V. Lakshmi, T. Chan and S.V. Nghiem (2003), Soil moisture retrieval from AMSR-E, *IEEE TGRS*, *41*, 215–229.

Pellarin,T., J.-P. Wigneron, J.-C. Calvet, and P. Waldteufel (2003), Global soil moisture retrieval from a synthetic L-band brightness temperature data set, *Journal of Geophysical Research (Atmospheres)*, *108*, ??? – ???.

J. T. Pulliainen, J. T., M. T. Hallikainen, and J. Grandell (1999), Hut snow emission model and its applicability to snow water equivalent retrieval, *IEEE Trans. Geos. Remot. Sens*, *37*, 1378–1390.

Reichle, R. and R.D. Koster (2004), Bias reduction in short records of satellite soil moisture, *Geophys. Res. Lett.*, *31*, L19501, doi:10.1029/2004GL020938.

Reichle, R. and R.D. Koster (2005), Global assimilation of satellite surface soil moisture retrievals into the NASA catchment land surface model, *Geophys. Res. Lett.*, *32*, L02404, doi:10.1029/2004GL021700.

Salgado, R. (1999), Global soil maps of sand and clay fractions and of the soil depth for MESONH simulation based on FAO/UNESCO soil maps, *CNRS/Meteo-France, Tech. Note*, *59*, ??? pp.

Seuffert, G., H. Wilker, P. Viterbo, M. Drusch, and J. Mahfouf (2004), On the usage of screen level parameters and microwave brightness temperature for soil moisture analysis, *J. Hydromet.*, *5*, 516–531.

Seuffert, G., H. Wilker, P. Viterbo, J. Mahfouf, M. Drusch, and J.-C. Calvet (2003), Soil moisture analysis combining screen-level parameters and microwave brightness temperatures: A test with field data, *Geophys. Res. Let.*, *30*, 10.1029/2003GL017144.

Ulaby, F.T., R.K. Moore, and A.K.Fung (1986), Microwave remote sensing: From active to passive. Part 3. From theory to applications, *Artech House*

Uppala, S.M., and 45 co-authors (2005), The ERA-40 re-analysis, *Quart. J. Roy. Met. Soc.*, *131*, 2961–3012.

van de Griend, A.A. and J.P. Wigneron (2004), The b-factor as a function of frequency and canopy type at h-polarization, *IEEE Trans. Geos. Remot. Sens*, *42*, 786–794.

van den Hurk, B.J.J.M., P. Viterbo, A.C.M. Beljaars, and A.K. Betts (2000), Offline validation of the ERA40 surface scheme, *Technical Memorandum 295*, *[Available through ECMWF, Reading, UK]*, 42pp.

Wigneron, J.P., A. Calvet, J.C. Chanzy and N. Bruguier (1995), A simple algorithm to retrieve soil moisture and vegetation biomass using passive microwave measurements over crop fields, *Rem. Sens. Env.*, *51*, 331–341.

Wigneron, J.P., L. Laguerre, and Y.H. Kerr (2001), A Simple Parmeterization of the L-band Microwave Emission from Rough Agricultural Soils, *IEEE Trans. Geos. Remot. Sens*, *39*, 1697–1707.

Njoku, E.G., T.J. Jackson, V. Lakshmi, T. Chan and S.V. Nghiem (2003), Soil moisture retrieval from AMSR-E, *IEEE TGRS*, *41*, 215–229.

Reichle, R. and R.D. Koster (2004), Bias reduction in short records of satellite soil moisture, *Geophys. Res. Lett.*, *31*, L19501, doi:10.1029/2004GL020938.

Reichle, R. and R.D. Koster (2005), Global assimilation of satellite surface soil moisture retrievals into the NASA catchment land surface model, *Geophys. Res. Lett.*, *32*, L02404, doi:10.1029/2004GL021700.

Seuffert, G., H. Wilker, P. Viterbo, M. Drusch, and J. Mahfouf (2004), On the usage of screen level parameters and microwave brightness temperature for soil moisture analysis, *J. Hydromet.*, *5*, 516–531.

Seuffert, G., H. Wilker, P. Viterbo, J. Mahfouf, M. Drusch, and J.-C. Calvet (2003), Soil moisture analysis combining screen-level parameters and microwave brightness temperatures: A test with field data, *Geophys. Res. Let.*, *30*, 10.1029/2003GL017144.

Ulaby, F.T., R.K. Moore, and A.K.Fung (1986), Microwave remote sensing: From active to passive. Part 3. From theory to applications, *Artech House*

B. J. Choudhury, T. J. Schmugge, A. Chang, and R. W. Newton. Effect of surface roughness on the microwave emission from soils. *J. Geophys. Res.*, 84:5699–5706, 1979.

B. J. Choudhury, T. J. Schmugge, and T. Mo. A parameterization of effective soil temperature for microwave emission. *J. Geophys. Res.*, 87:1301–1304, February 1982.

R.B. Clapp and G.M. Hornberger. Empirical equations for some hydraulic properties. *Water Res. Res.*, 14: 601–604, 1978.

B.J. Cosby, G.M. Hornberger, R.B. Clapp, and T.R. Ginn. A statistical exploration of the relationships of soil moisture characteristics to the physical propoerties of soils. *Water Res. Res.*, 20:682–690, 1984.

DeVries. Heat transfer in soils. In D.A. DeVries and N.H. Afgan, Wiley, editor, in *Heat and mass transfer in the biosphere. Part I: Transfer processes in the plant environment*, 4–28, 1975.

ECMWF. Integrated Forecast System Documentation. [Available online at http://www.ecmwf.int/research/ifsdocs/], 2003.

et al. Hallikainen. ESTEC CONTRACT, NO 11706/95/NL/NB(SC), FINAL REPORT. -, pages 60–68, 1995.

Daniel Hillel. *Fundamentals of soil physics*. Acad. Press New York, 1980.

T. R. H. Holmes, P. de Rosnay, R. de Jeu, R. J.-P. Wigneron, Y. Kerr, J.-C. Calvet, M. J. Escorihuela, K. Saleh, and F. Lemaître. A new parameterization of the effective temperature for L band radiometry. *Geophy. Res. Letters*, 33:7405–+, April 2006.

T. J. Jackson and T. J. Schmugge. Vegetation effects on the microwave emission of soils. *Remote Sensing of Environment*, 36:203–212, 1991.

Jackson, T.J., A.Y. Hsu, A. Van de Griend, and J.R. Eagleman (2004), Skylab L-band microwave radiometer observations of soil moisture revisited, *Int. J. Rem. Sens.*, *25*, 2585–2606.

Y.H. Kerr and E.G. Njoku. A semiempirical model for interpreting microwave emission from semiarid land surfaces as seen from space. *IEEE Trans. Geos. Remot. Sens*, 28 (3):384–393, 1990.

K. P. Kirdiashev, A. A. Chukhlantsev, and A. M. Shutko. Microwave radiation of the earth's surface in the presence of vegetation cover. *Radiotekhnika i Elektronika.*, 24:256–264, 1979.

L. A. Klein and C. T. Swift. An improved model for the dielectric constant of sea water at microwave frequencies. *IEEE Trans. Anten. and Propag.*, AP-25(1):104–111, 1977.

H. J. Liebe. MPM- An atmospheric millimeter-wave propagation model. *Int. J. Infrared Millimeter Waves*, 10: 631–650, 2004.

V. Masson, J.-L. Champeaux, F. Chauvin, C. Meriguet, and R. Lacaze. Ecoclimap, a global database of land surface parameters at 1km resolution in meteorological and climate models. *EGS - AGU - EUG Joint Assembly, Abstracts from the meeting held in Nice, France, 6 - 11 April 2003, abstract #8782*, pages 8782–+, April 2003.

C. Matzler. Microwave permittivity of dry sand. *IEEE Trans. Geos. Remot. Sens*, 36(1):317–319, 1998.

K.A. Patterson. Global distribution of total and total-available soil water-holding capacities. M.S. Thesis, pages Department of Geography, University of Delaware, 1990.

T. Pellarin, J.-P. Wigneron, J.-C. Calvet, and P. Waldteufel. Global soil moisture retrieval from a synthetic L-band brightness temperature data set. *Journal of Geophysical Research (Atmospheres)*, 108:9–1, June 2003.

C.D. Peters-Lidard, E. Blackburn, X. Liang, and E.F. Wood. The effect of soil conductivity parameterization on surface energy fluxes and temperature. *J. Atmos. Sci.*, 55:1209–1224, 1998.

J. T. Pulliainen, M. T. Hallikainen, and J. Grandell. Hut snow emission model and its applicability to snow water equivalent retrieval. *IEEE Trans. Geos. Remot. Sens*, 37:1378–1390, 1999.

A. Stogryn. Equations for calculating the dielectric constant of saline water. *IEEE Trans. Microw. Theory. Techn.*, MTT-19:733–736, 1971.

F.T. Ulaby, R.K. Moore, and A.K. Fung. *Microwave Remote Sensing*, volume III. Artech House. Inc., 1986.

U.S. Geological Survey. Global Land Cover Characterization. [Available online under http://edcsns17.cr.usgs.gov/glcc/] , 1999.

B.J.J.M. van den Hurk, P. Viterbo, A.C.M. Beljaars, and A.K. Betts. Offline validation of the ERA40 surface scheme. Technical Memorandum 295, 42 pp:[Available through ECMWF, Reading, UK], 2000.

P. Viterbo. The representation of surface processes in General Circulation Models. PhD Thesis, 201 pp: [Available through ECMWF, Reading, UK], 1996.

P. Viterbo and A.C.M. Beljaars. An improved land surface parameterization scheme in the ECMWF model and its validation. Technical Report 75, 58 pp:[Available through ECMWF, Reading, UK], 1995.

J. R. Wang and B. J. Choudhurry. Remote sensing of soil moisture content over bare field at 1.4 ghz frequency. *J. Geophys. Res.*, 86(C6):5277–5287, 1981.

J. R. Wang and T. J. Schmugge. An empirical model for the complex dielectric permittivity of soils as a function of water content. *IEEE Trans. Geos. Remot. Sens*, 18(4):288–295, 1980.

U. Wegmueller and C. Matzler. Rough bare soil reflectivity model. *IEEE Trans. Geos. Remot. Sens*, 37(3): 1391–1395, 1999.

U. Wegmueller, C Matzler, and Njoku E.G. *Canopy opacity models*, page 375. In: Passive Microwave remote sensing of land-atmosphere interactions, B.J. Choudhury et al. (eds.), VSP, Utrecht, The Netherlands, 1995.

J.P. Wigneron, A. Calvet J.C. Chanzy, and N. Bruguier. A simple algorithm to retrieve soil moisture and vegetation biomass using passive microwave measurements over crop fields. *Remote Sensing of Environment*, 51:331–341, 1995.

J.P. Wigneron, L. Laguerre, and Y.H. Kerr. A Simple Parmeterization of the L-band Microwave Emission from Rough Agricultural Soils. *IEEE Trans. Geos. Remot. Sens*, 39:1697–1707, 2001.

T. T. Wilheit. Radiative transfer in a plane stratified dielectric. *IEEE Trans. Geos. Electr.*, 16(2):138–143, 1978.

Wilker, H., M. Drusch, G. Seuffert, and C. Simmer (2006), Effects of the near-surface soil moisture profile on the assimilation of L-band microwave brightness temperature, *J. Hydromet.*, *??*, ????–????.